Green Chemistry

PAPER

View Article Online
View Journal

Cite this: DOI: 10.1039/d6gc00237d

Mechanistic insights into hydrothermal carbon formation: from biomass to pyrolyzed carbons with enhanced interparticle connectivity for energy-related applications

Melina Müller, [a] Michael Poschmann,[a] Markus Leutzsch, [b] Walid Hetaba, [a] Thomas Weyhermüller,[a] Adib Caidi,[c] Ivan Radev,[c] Kristina Tschulik [d] and Saskia Heumann *[a]

Hydrothermal carbonization (HTC) is widely regarded as a sustainable route for converting biomass into carbon materials; however, the formation mechanisms of structurally diverse biomass feedstocks remain insufficiently understood. This work systematically investigates HTC reaction pathways of both solid and liquid products using wheat straw (second-generation biomass), wet corn gluten feed (first-generation by-product), and sugars as model systems under varying pH, temperature, and residence time, while directly linking structural evolution of the solids to their electrochemical applicability. A key novelty is the comprehensive, quantitative analysis of liquid filtrates by 1D- and 2D-NMR spectroscopy, enabling access to possible green platform chemicals (levulinic acid, 3-hydroxypyridine, furfurals) as well as considerations regarding toxicology for downstream processing. 3-Hydroxypyridine derivatives form the main N-containing molecular motif in the filtrate, likely formed *via* Strecker degradation of amino acids with C5-sugar-derived diketones—confirmed through model reactions of C5 and C6 sugars with glycine. Overall, HTC as a pretreatment before pyrolysis increases the carbon content, sp^2/sp^3 ratio, and bulk conductivity due to increased interparticle connectivity of sugar-derived hydrochar, while reducing alkali contaminants (<0.1 wt%) compared to direct pyrolysis of the biomass. As a proof of concept, selected pyrolyzed carbons are decorated with Pt nanoparticles and exhibit oxygen reduction reaction activity, electrochemical surface area, and kinetic currents approaching those of commercial Pt/C catalysts on a rotating disk electrode, indicating their potential as catalyst supports while highlighting the surface area–conductivity trade-off that limits their applicability.

Received 13th January 2026,
Accepted 29th April 2026

DOI: 10.1039/d6gc00237d

rsc.li/greenchem

Green foundation

1. This work provides a fundamental understanding of biomass conversion pathways during hydrothermal carbonization and pyrolysis that enables the design of more efficient, less wasteful processes, particularly those related to renewable feedstocks, energy efficiency, and waste prevention.
2. Specific green achievements using hydrothermal carbonization: novel detailed NMR analysis of HTC filtrate products enables potential valorization to sustainable platform chemicals. Agricultural waste streams are utilized as renewable feedstocks. Fuel cell catalysts with electrochemical properties comparable to petroleum-derived commercial catalysts are produced.
3. Identification of 3-hydroxypyridine and other nitrogen-containing compounds in the filtrate opens opportunities for developing catalytic processes to convert these compounds into valuable platform chemicals, rather than treating them as waste. Research could explore additional agricultural waste streams with high protein content to maximize waste utilization and reduce the environmental footprint. Further research could explore methods to reduce or replace Pt loading while maintaining performance.

[a]*Max-Planck-Institute for Chemical Energy Conversion, Stiftstraße 34-36, 45470 Mülheim an der Ruhr, Germany. E-mail: saskia.heumann@cec.mpg.de*
[b]*Max-Planck-Institut für Kohlenforschung, Kaiser-Wilhelm-Platz 1, 45470 Mülheim an der Ruhr, Germany*
[c]*The Hydrogen and Fuel Cell Center (ZBT GmbH), Carl-Benz-Strasse 201, 47057 Duisburg, Germany*
[d]*Faculty of Chemistry and Biochemistry, Chair of Analytical Chemistry, Ruhr University Bochum, 44801 Bochum, Germany*

Introduction

The functionalization of biomass, comprising plant, animal, and anthropogenic waste, is key to a carbon-neutral, circular economy.[1] Lignocellulosic feedstocks can exhibit a complex structure dominated by cellulose, hemicellulose, lignin, protein and ash requiring intensive pretreatment, but offer

improved environmental compatibility due to their abundance and non-food nature. Conversion techniques like hydrothermal carbonization (HTC),[2] pyrolysis,[3] and enzymatic conversion[4] are topics of research and employed industrially to retrieve gaseous, liquid and solid products (*e.g.*, biogas, alcohol, and charcoal, respectively). The transformation of cheap and available agricultural and other anthropogenic waste into higher value carbon materials is already industrially implemented by HTC companies[5–8] and is viable if the disposal of the waste by incineration is costly or if the alternative is environmentally harmful (open-field burning, landfilling or the use of petroleum-based products).

During HTC, the organic matter is reformed in the presence of subcritical water, which exhibits its maximum ionic product at temperatures between 180 and 300 °C and under self-generated pressure, into a solid product (hydrochar) with an increased carbon content and reformed surface chemistry.[9,10] An advantage of HTC is that no energy-extensive drying is needed, with even high moisture contents being favorable.[11]

During the process, components of the biomass are dissolved into the aqueous phase where generally hydrolysis of the extractives, hemicellulose, and amorphous cellulose occurs first, followed by dehydration, decarboxylation, condensation, and polymerization, which leads to a pressure-generating gas phase (mostly CO_2), the solid hydrochar and a complex liquid.[16] Aldol condensation and ring-opening reactions of aqueous hydroxymethylfurfural (HMF) and furfural form the secondary solid products and define the surface morphology of sugar-derived HTC spheres.[17,18] These solids exhibit a core–shell structure likely formed through dehydration-driven growth, with β-linked furanic domains and arene clusters in the core, while the surface is enriched in carboxyl and aldehyde groups.[19,20] The liquid, the so-called biocrude, contains sugars and sugar-derived compounds such as HMF, furfural, phenol derivatives, and organic acids, in concentrations depending on the reaction time and temperature.[21] Molecules such as levulinic acid,[22] HMF[23] and furfurals[24,25] are seen as possible candidates for further transformation into bio-based fine chemicals. The process liquor is often analyzed by High-Performance Liquid Chromatography (HPLC) for the quantification of sugars/acids and Gas Chromatography coupled with Mass Spectrometry (GC-MS) for identifying aromatic and volatile degradation products, though the information on the structural details of unknown compounds in complex mixtures can be limited.[26–28] Nuclear Magnetic Resonance (NMR) spectroscopy has been utilized for analysis of the main components of biocrude and pyrolysis process liquors, since it is a fast method for quantification and enables the structural characterisation of unknown components directly from the mixtures.[29–33] With this work, we addressed the current lack of detailed, pH-dependent NMR chemical shift data of biomass-derived products found in the filtrate, which go beyond well-known main products. Implication of the findings can be important for the safety and also utilization of HTC process liquors. Due to the presence of amino acids and inorganic nitrogen salts in most biomasses, nitrogen-doped hydrochar with both bulk and surface N-functionalities are formed *via* the Maillard reactions of sugars with amino acids.[34–36] The hydrochar is often characterized by elemental analysis and X-ray Photoelectron Spectroscopy (XPS). The filtrate is rarely analyzed for nitrogen compounds, which are investigated in this work using $^{1}H–^{15}N$-HMBC experiments. With the information gained from component analysis with NMR, we shed light on the role of individual components of biomass (cellulose, hemicellulose, lignin, starch, protein) and how HTC as a pretreatment affects the chemical structure of the resulting pyrolyzed carbon material (Fig. 1).

Due to the enhanced energy and mass density, hydrochar as such is a candidate for use as a solid fuel[9] and fertilizer[37] in agricultural applications. The meso- to microporous structure of HTC-treated biomass[38] can be retained during the pyrolysis to amorphous (T < 1200 °C) or graphitic (T > 1200 °C) carbons,[39] which can serve as activated carbon in water purification,[40] electrode materials in batteries,[41,42] supercapacitors,[43] and support materials for nanoparticles in fuel cell applications.[44] The functional groups on the surface of the carbon can act as anchoring points for metal centers and particles,[45] and can be tailored by adding dopants like N-sources into the HTC process.[46] To be viable for electrochemical applications such as fuel cells, carbon materials must meet high standards to compete with petroleum-derived carbons like carbon black. In addition to high purity and chemical stability (low carbon corrosion), they require an optimal surface area (meso- to macroporous morphology) and uniform dispersion of catalyst nanoparticles (*e.g.*, Pt/Pt alloys or non-precious metals), which must be well stabilized to prevent agglomeration or degradation.[47,48] In the membrane assembly of a fuel cell, an ionomer (*e.g.*, Nafion) is used to enable proton transfer to the active metal sites. Surface functional groups on the carbon affect ionomer interaction, with optimal hydrophilicity promoting adsorption.[49] Nitrogen functionalization can enhance acid–base interactions between N-moieties and $–SO_3^-$ groups of Nafion.[50,51] In the case of the biomass-derived carbons, nitrogen functionalization is achieved naturally due to the presence of amino acids. However, electrochemical performance depends largely on the interplay of the aggregate structure (catalyst building blocks where ionomer adsorbs) and electrochemical surface area (ECSA).[52] Ink formulation strongly influences catalyst layer (CL) performance: solvent polarity alters the agglomerate structure, with low polarity promoting Nafion desorption and carbon agglomeration, and high polarity enhancing dispersion.[53] Thus, the ink composition must be tailored to the surface chemistry of the carbon support prior to membrane electrode assembly (MEA). Another critical factor is bulk conductivity, since CL resistance impacts ohmic losses of the stack. Given the limited data on annealed HTC-derived carbons compared to commercial supports such as Vulcan XC72, early-stage conductivity screening is needed to identify suitable materials. As a proof of concept, HTC-treated biomass with promising properties and Vulcan XC72 were decorated with Pt nanoparticles *via* chemical deposition and compared to a commercial Pt–carbon black catalyst.

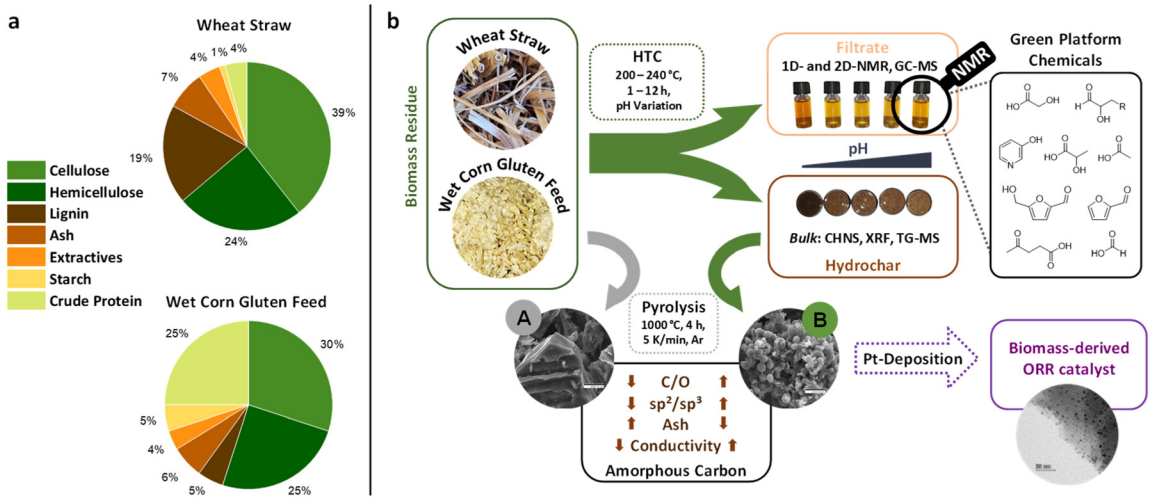

Fig. 1 (a) Main macromolecular components of used biomass for HTC studies averaged from different sources[12–15] and (b) overview of applied HTC reaction conditions and analysis methods with qualitative and quantitative NMR of the liquid filtrate, providing insights into toxicity for downstream processing and possible green platform chemicals. The HTC-treated, pyrolyzed hydrochar A is compared to a directly pyrolyzed biomass B, and the most promising amorphous carbons are decorated with Pt nanoparticles. These biomass-derived ORR catalyst are tested for preliminary kinetic performance on the RDE and compared to petroleum-sourced, commercial Pt on carbon black.

Their ORR activity was tested on a rotating disk electrode (RDE) in 0.1 M $HClO_4$. Although RDE offers only limited insight into catalyst stability due to the very different catalysis conditions (RDE: immersed in acidic solution, MEA: humid O_2 gas),[54] it remains valuable for assessing ECSA *via* hydrogen-underpotential deposition (H-UPD) and ORR kinetics[55] to evaluate the feasibility of HTC-treated biomass as a Pt support for the ORR.

Results and discussion

To compare sugar-derived HTC materials with biomass, hydrothermal treatments were carried out at 200 °C with different residence times. A full description of reaction conditions is provided in the SI. Briefly, 3.5 g of sucrose was dissolved in 30 mL of distilled water, while wet biomass samples (wet corn gluten feed: 5 g ≈ 2 g dry mass; WS: 2.5 g ≈ 2.3 g dry mass) were shredded into 3–6 mm flakes and immersed in 30 mL of distilled water inside a Teflon liner. A solid hydrothermal carbon and a liquid filtrate were obtained after reaction.

Filtrate analysis with time variation

For NMR analysis, 300 µL of the filtrate were combined with 50 µL of a maleic acid standard solution (~20 mg mL^{-1}) and 350 µL of D_2O. Quantitative data were obtained from ^1H spectra using maleic acid as a suitable standard[56] and 2D experiments were done for structure identification. Detailed descriptions of the NMR experimental settings to obtain quantitative data, errors of the method, chemical shifts of all identified molecules, and the peaks used for integration can be found in the SI. The C and N mass balance of the HTC process was estimated using elemental analysis and XRF of the hydrochar and NMR analysis of soluble filtrate components (Tables S12–14). The unaccounted fractions (here referred to as 'losses') are attributed to complex aqueous oligomers, such as humins, which may remain in the hydrochar but are washed out during filtration, or persist in solution without being individually quantifiable by NMR. In addition, a minor fraction is lost to the gaseous headspace, which typically accounts for 5–10% of the mass (predominantly CO_2)[57,58] in HTC processes. Overall, 20–40% of the mass (depending on process conditions, see the SI) is likely associated with macromolecular species that do not contribute to the solid yield. As these fractions cannot be structurally resolved and the gaseous phase was not analyzed, the calculated atom efficiencies should be considered approximate.

Sucrose, composed of α-1,2-glycosidically linked D-glucose and D-fructose, hydrolyzed readily under HTC conditions. After 1 h at 200 °C (excluding the heating ramp of 5 °C min^{-1}), a mixture of glucose and fructose anomers was detected together with the first formation of HMF (Fig. S4 and S5; ^1H–^{13}C HSQC of the sugar isomers and HTC filtrate). The formation of HMF from D-fructose is a well-known reaction and its first-order kinetics and mechanisms have been thoughly studied by many groups.[59,60] Under acidic conditions, HMF further reacts to form levulinic acid and formic acid, which readily happens under HTC conditions due to the increased ionic product of water (Scheme S1, mechanism from D-glucose isomerization to levulinic acid). During the reaction, progressive acid formation lowered the pH to ~2, which further promoted sugar dehydration and levulinic acid production. Nevertheless, complete sucrose consumption (starting conentration 4 g per 30 mL) was not achieved at 200 °C, as D-glucose signals were still observed after 12 h. On the right-hand *Y*-axis of Fig. 2a, the total concentration [mmol $g_{biomass}^{-1}$

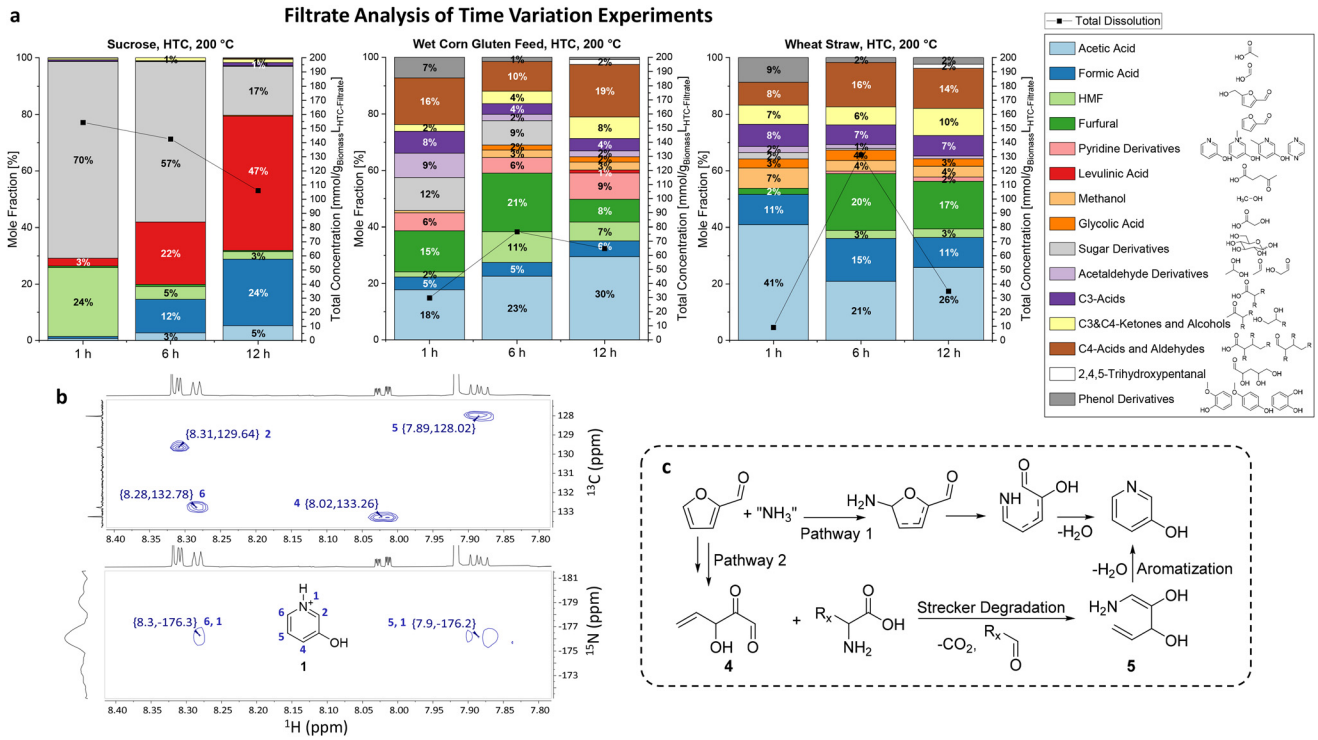

Fig. 2 HTC time variation experiments at 200 °C of sucrose, WCGF and WS with filtrates analyzed by NMR (approx. error: 1–5%, see the SI). (a) Molar fractions of identified molecules in % (left *Y*-axis) and the total molar concentration of molecules in mmol $g_{biomass}^{-1}$ $L_{HTC\text{-}filtrate}^{-1}$ with 4 g of wet biomass or sugar in 30 mL of dest. H_2O (right *Y*-axis). (b) $^{1}H–^{13}C$-HSQC and $^{1}H–^{15}N$-HMBC spectra (referenced to $MeNO_2$) of 3-hydroxypyridine found in the WCGF filtrate after 12 h, measured at 600 MHz in $H_2O:D_2O$. (c) Proposed mechanism of furfural and ammonia (pathway 1) and Strecker degradation (pathway 2) of diketone **4** derived from furfural to form the observed 3-hydroxypyridine.

$L_{HTC\text{-}filtrate}^{-1}$] gives an indication of the concentration of dissolved molecules in solution. This parameter is directly complementary to the solid yield of hydrochar, since a lower degree of total concentration corresponds to a higher solid yield, and conversely, higher dissolution results in a reduced amount of hydrochar (solid yield data in Fig. S17, S18, S20, and S22). The gradual decrease observed after 6 h across all samples can be attributed to the polymerization of HMF and furfural, which progressively condense to form the solid hydrochar residue.[61,62] The filtrate analysis showed that the dissolution behavior of biomass follows a volcano-shaped trend: initially, hydrolyzable and soluble components leach out, after which part of these species repolymerize to form hydrochar. After one hour at 200 °C, short amylose chains consisting of 15 units of α-1,4-D-glucose (identified in the ^{1}H anomeric and glycosidic proton region between 5.0 and 5.5 ppm, see Fig. S6) were observed in the filtrate of wet corn gluten feed (WCGF), consistent with its high starch content. Shorter reaction times are often used when sugar extraction from biomass is the incentive; here, HMF generation and furfural generation are seen as competing reactions.[63] Wheat straw shows high dissolution of acetic acid, attributed to cleavable acetyl side chains of hemicellulose, but lower sugar yields, as effective leaching requires higher temperatures due to sugars being bound in amorphous and crystalline cellulose embedded within lignin and hemicellulose. Lignin and highly crystalline cellulose decompose only partially, forming micro-sized rounded fragments that undergo primarily solid–solid transformations,[64] which, together with the limited water penetration through the hydrophobic lignin network, necessitates higher decomposition temperatures and longer reaction times compared to dissolved sugar model systems. The compositional changes of the resulting hydrochar over temperature and time are summarized in Fig. S17, S18, S20, and S22 and the pH changes in the filtrate are shown in Tables S8–S10. Consistent with previous reports, the C/O ratio increases over time for the sugar model system and sugar-rich biomass,[19] threefold for sucrose and twofold for WCGF, while for wheat straw no significant increase was detected at 200 °C, indicating that substantial dehydration occurs only at higher temperatures. After 6 h, the alkali metal concentration in biomass-derived hydrochar decreased to below ≈0.1 wt%, and the silicon content in wheat straw was reduced from 6 wt% to 2 wt%, which is still above acceptable levels for applications requiring pure carbon materials. The negative consequences on properties are discussed in the section on the pyrolyzed carbon materials and the conclusion. Notably, the solid yield of WCGF was already reduced to 44% after 1 h, whereas wheat straw retained 91% of its original dry matter (Fig. S17). The trend can be understood when looking at the total

Table 1 Proximate analysis adapted from ASTM D7582 Standard Test Method and elemental CHNSO analysis of used biomass (error in the SI)

Biom./wt%	Fixed carbon	Volatiles	H_2O	Ash	C	H	N	S	O[a]
WS	24 ± 2	57 ± 4	7 ± 4	12 ± 3	45	6	0.3	0.4	39
WCGF	30 ± 2	9 ± 1	60 ± 2	1.0 ± 0.5	47	7	2	0.5	44

[a] Calculated by difference.

concentration in a different unit [mg $mL_{HTC\text{-}filtrate}^{-1}$] (Fig. S16). The heavy amylose chains that are dissolved, as well as the high original water content of the WCGF (Table 1), likely lead to better wettability and accessibility for aqueous degradation, resulting in the high early mass loss in the solid. This can also be seen in the onset of formation of furfural stemming from C5 sugars present in hemicellulose. Phenolic compounds are prominent in the filtrate after 1 h, but their concentration decreases over time, indicating their involvement in repolymerization processes that contribute to the formation of secondary char. These early-released phenolics are likely derived from xylan units within hemicellulose, which consist of a β-1,4-D-

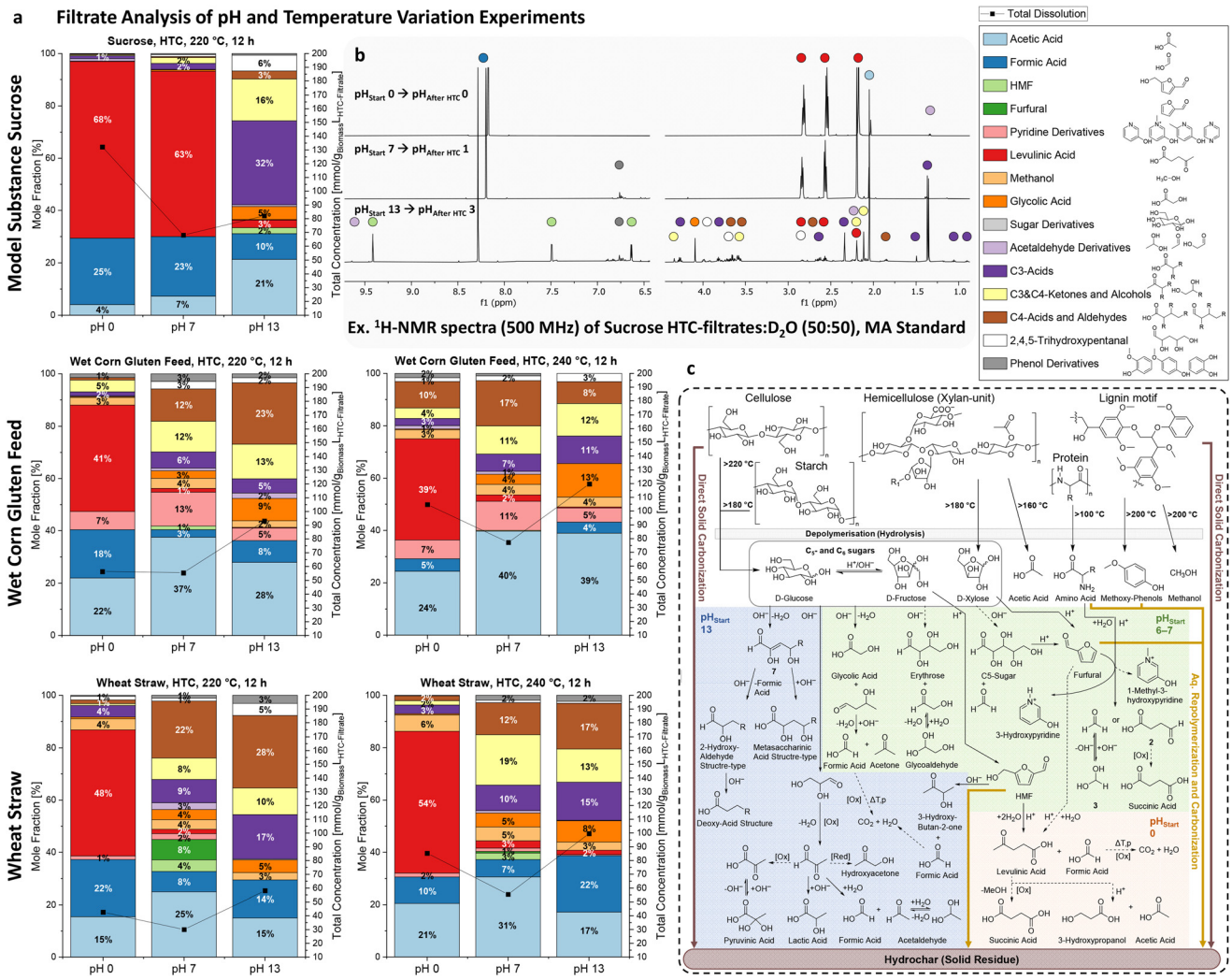

Fig. 3 (a) HTC starting pH variation experiments at different temperatures (reaction time: 12 h) of sucrose, WCGF and WS filtrates analyzed by NMR (approx. error: 1–5%, see the SI). Mole fractions of identified molecules in % (left *Y*-axis) and the total concentration of molecules in mmol $g_{biomass}^{-1}$ $L_{HTC\text{-}filtrate}^{-1}$ with ~4 g of wet biomass or sugar in 30 mL of dest. H_2O (right *Y*-axis). The pH on the *X*-axis refers to the starting pH, where pH 0 was adjusted with 0.1 M HNO_3 and pH 13 with 0.1 M KOH. (b) ^{1}H-NMR spectra of sucrose filtrates after 12 h at 220 °C with different pH_{start} measured at 500 MHz in H_2O : D_2O. (c) Proposed mechanistic overview of the main components in biomass (enlarged in Scheme S9). Molecules that were identified *via* NMR are named in the scheme; non-observed but reasonable intermediates are marked with a number or are unnamed. Dashed arrows imply that the product formation was observed in minor amounts.

xylose backbone that can be acetylated or substituted with α-L-arabinofuranose side chains. The latter may be further esterified with ferulic acid (Fig. 3c, xylan unit R_1), which provides a covalent linkage between hemicellulose and lignin in certain plant cell wall species.[65]

Pyridine formation in filtrates

Interestingly, in the WCGF filtrate, over time, the production of protonated 3-hydroxypyridine as one of the main products can be observed (Fig. 2b, ^{1}H–^{13}C HSQC and ^{1}H–^{15}N HMBC). Wheat straw produces small amounts of 3-hydroxypyridine as well, but the mole fraction never exceeds 2% for the experiment conditions used in this paper. Since WCGF contains high amounts of protein (Fig. 1a) and almost 7-times higher N wt% compared to wheat straw (Table 1), it is not surprising to find Maillard-reaction products in the HTC process liquid. Maillard reactions are a collection of reactions that are part of the browning process in food and essentially consist of the condensation of a reducing sugar with an amino acid compound. 3-Hydroxypyridine could be formed by the Strecker degradation described in Fig. 2c pathway 2 (in detail in Scheme S4a), where the acid-catalyzed degradation product of furfural, 1,2-diketone **4** (formation of diketones from sugars in Schemes S1 and S2), and an amino acid form an imino acid.[34,66] After decarboxylation and upon the addition of water, an aldehyde with the rest-chain depending on the original amino acid and amine **5** can be formed, which can aromatize to 3-hydroxypyridine. The Strecker degradation product of the 1,2-diketone generated from C6-sugar derived HMF and an amino acid is 3-hydroxy-6-methyl-pyridine (Scheme S3), which can only be observed in WCGF-derived filtrates making up between 0 and 14.5% of the N-compounds found in the solution depending on the starting pH (Tables S5 and S6). However, twice the amount of 1-methyl-3-hydroxypyridine was found as a by-product in the WCGF filtrates making up 20–25% of the pyridine motifs, the rest being unmethylated 3-hydroxypyridine. 1-Methyl-3-hydroxypyridine likely originates from the condensation of the amine produced as a possible side product (Scheme S4b), indicated by the dashed arrow in Scheme S4a. This product would be the resulting pyridine if glycine was present as an amino acid. Another plausible formation pathway of 3-hydroxypyridine from furfural and ammonia was previously described by Ren *et al.*, over an RANEY® Fe catalyst (Fig. 3c, pathway 1),[67] which in the case of acidic hydrothermal conditions could be simply Brønsted acid catalyzed with ammonia formed by amino acid decomposition. The 3-hydroxypyridine motifs could also be verified in this specific filtrate by GC-MS (Fig. S13). We propose that HMF formed by C6-sugars is more likely to oxidize to levulinic acid and formic acid or degrade through different mechanisms, which will be discussed in detail in the next part of the paper (Fig. 3c, pH-dependent degradation mechanisms). To confirm this hypothesis, model system experiments with D-xylose (C5-sugar) and D-glucose (C6-sugar) were done by adding glycine as an amino acid source. The filtrates of D-xylose showed a pyridine-derivative concentration [mmol $g_{biomass}^{-1}$ $L_{HTC\text{-}filtrate}^{-1}$] 5.5 times higher than in the D-glucose filtrates (Fig. S14). Interestingly, for D-xylose filtrates, the molar fractions of 3-hydroxypyridine were ≈9.1% and of 1-methyl-3-hydroxypyridine ≈6.7%, and additionally ≈1.6% of pyrazine could be identified. Pyrazine is known to be formed from the Amadori compound of sugars *via* recondensation of fractionated α-amino carbonyls (Scheme S5, formation of the Amadori compound).[68] The D-glucose filtrates exhibit additional peaks, assigned to the C6-expected product 6-methyl-3-hydroxypyridine, which, at ≈1.6%, had the highest molar concentration of the identified pyridines in this filtrate (Fig. S14, molecule content summary). The model system filtrates were analyzed by GC-MS as well (Fig. S13). Another noteworthy trend was that the solid yield of D-xylose derived hydrochar was 5% lower and also had 8% lower nitrogen built into its carbon matrix (Table S7), which stresses again the need for analyzing both the filtrate and solid product to understand the formation mechanisms. Although the Maillard reaction encompasses many possible reaction pathways, the 3-hydroxypyridine motif consistently emerged as the most prominent product under the applied range of HTC process conditions. It seems that D-glucose undergoes other decomposition reactions that do not lead to a heavy formation of the pyridine Strecker analog, and builds in nitrogen more readily into its hydrochar than D-xylose. The formation of the 3-hydroxypyridine motif has been described before in buffered glucose–ammonia systems in methanol,[69,70] but to the best of our knowledge has not been reported in previous HTC studies of biomass and can be useful for deducing new bio-based platform chemicals and also for assessing the toxicity of filtrates.

Filtrate analysis with pH variation

A pronounced difference is observed between the filtrate compositions of the sucrose model system and the biomass: although sugars are leached from the biomass, little to no levulinic acid is detected in its filtrates obtained after hydrothermal processing at 200 °C. Instead, large amounts of C3 and C4 acids and aldehydes can be found along with glycolic acid and methanol likely originating from hydrolysis of methoxylated side chains of lignin. The results show that one contributing factor is the autocatalysis resulting from pH reduction when sugar is readily available. For sucrose, the initial pH drops to 3 during 6 h and to 2 during 12 h, facilitating both acid-catalyzed levulinic acid formation and polymerization of furans into secondary char. In contrast, since sugars must first leach from biomass, the initial pH of the filtrates remains higher, at 4.5 and 5 after 6 h and 4 and 5 after 12 h for WCGF and wheat straw, respectively. This higher pH allows other non-acid-catalyzed reactions to proceed, resulting in a more diverse molecular composition in the biomass filtrates. To further investigate the influence of pH on the filtrate composition and hydrochar formation, experiments were conducted at 200, 220 and 240 °C with starting pH values of 0, 7 and 13, adjusted by adding 0.1 M HNO_3 or KOH to the biomass and model system. The starting pH is the pH of the solution before being mixed with the biomass; for sugar

model systems, pH_{start} is the same as pH_{mixed} as the pH does not change. pH_{end} is the pH of the filtrate after HTC (Tables S7–S11, pH change of filtrates). Representative ^{1}H–^{13}C HSQC spectra of the most challenging filtrates, biomass at initial pH 7 and sucrose at pH 13, are shown in Fig. S8–S10 to assist in resolving overlapping peaks in the ^{1}H NMR spectra (Fig. 3b).

It becomes clear that lowering the pH for sucrose does not bring an advantage if one is interested in obtaining hydrochar, because the high levulinic acid production outcompetes the polymerization reaction and leads to lower solid yields with no clear benefit in carbon wt% content in the hydrochar. It should be mentioned that at 240 °C, the addition of HNO_3 in sucrose led to N-functionalization of the hydrochar (0.5 wt%; Fig. S22), whereas in the biomass samples, the N-content seems not to be significantly influenced by HNO_3 but mainly from original amino acid content. When looking at the influence of starting with a high pH, the content contributions start to look similar to those of the biomass, since the fast lowering of pH is inhibited by buffering of OH^- ions in solution; as for the biomass, the concentration of available degrading sugar in solution is never high enough to reach the level of autocatalysis of non-buffered sucrose solution. The following paragraph can be best understood in conjunction with the mechanistic overview shown in Fig. 3c and the detailed mechanisms in the SI. If a molecule is identified by NMR, it is named in the scheme. Dashed reaction arrows imply that the product was not found in large amounts compared to the main products. We would like to highlight the finding of the expected base-catalyzed degradation product with a metasaccharinic structure (Scheme S6, pathway 3.1),[71] but also 2-hydroxy-3-deoxy-aldehyde structures and their corresponding oxidized acids, which form *via* hydride shift of the dihydroxy product and elimination of the β-hydroxy group (Scheme S6, pathway 2). Both likely stem from 3-deoxyglucosone that is often observed as an intermediate in the case of C6-sugar degradation. 3-Deoxyglucosone may form 2,3-dioxyglucosone-3-ene, which can isomerize to HMF, even though it is established that the open chain reaction to form HMF is not favored.[59] We propose that a significant portion of the high dissolution arises because, rather than forming HMF that can polymerize into secondary char, glucose is degraded into 2-hydroxy-3-deoxy-aldehyde structures and their corresponding oxidized acids, while other base-catalyzed pathways also generate metasaccharinic acid structures. Many shorter-chained forms of these product types are detected not only in biomass, where C5 sugars are inherently present, but also in the C6 sucrose sample. This suggests that sugars undergo retro-aldol reactions, producing glycolaldehyde and C4 erythrose or acetaldehyde and a C5 sugar (Scheme S7),[72] which can further degrade to yield the previously described C4 and C5 aldehydes and acids. The other important groups of degradation products are C3 acids and C3 & C4 ketones and alcohols. Lactic acid is commonly formed *via* C3–C4 retro-aldol cleavage (in the case of a C6 sugar) that results in the formation of two trioses, which can both form a diketone intermediate.[66] Benzilic rearrangement leads to the formation of lactic acid (Scheme S6, pathway 1), whereas a disproportionation *via* the Cannizzaro reaction can lead to pyruvic acid and hydroxyacetone (Fig. 3c). If instead of the benzilic rearrangement, no hydride transfer but a proton is added, the diketone is split into formic acid and acetaldehyde. Another reaction pathway that depletes HMF under basic starting conditions is its decomposition to 3-hydroxybutan-2-one and formic acid. This reaction could proceed similarly to the HMF-to-levulinic acid pathway, but instead of water or a hydroxide ion attacking the C2 atom (as in levulinic acid formation), the nucleophilic attack occurs at the C3 atom (Scheme S8). For both low and high starting pH, the increased formation of formic acid can be observed due to the reactions mentioned above yielding formic acid as a common product. Formic acid can decompose into CO_2 and water under hydrothermal conditions,[73] which leads to the self-pressurization of the HTC process. Only under inert conditions with a noble metal catalyst, could the formation of CO_2 and H_2 as HTC decomposition products be observed.[74] Succinic acid was detected in most filtrates, although its formation pathway is less clear than for the other compounds. It may originate from oxidized erythrose *via* a pathway analogous to that leading to 3,4,5-trihydroxypentanoic acid (Scheme S6, pathway 3.2). Supporting this hypothesis is the observation of 3-hydroxy-4-oxobutanoic acid as a possible intermediate in the filtrate of sucrose at starting pH 13 (Fig. S10, molecule **27**).

Acid catalyzed formation of levulinic acid takes away the yield from hydrochar in the case of pure sugar derived hydrochar. In the case of biomass, it seems to assist the formation of higher carbon containing hydrochar, bringing its carbon content closer to the model system at starting pH 7 (Fig. S18 and S20). More biomass is hydrolyzed which leads to a higher concentration of molecules in the filtrate but also to the formation of HTC spheres which have a higher carbonization degree due to the condensed furfural motifs. At a high starting pH, more components leach out as well but little to no HTC formation can be observed in the graphical morphology analysis *via* scanning electron microscopy (SEM) (Fig. 5a), which matches the mechanistic analysis discussed above. A further drawback of initiating the reaction at high pH is the retention of potassium within the carbon matrix, even after extensive washing. Achieving a pure carbon material therefore required washing the hydrochar with twice the volume of water compared to samples prepared at pH 0 and 7.

Increasing the HTC temperature leads to a carbon product with a higher degree of aromatization.[75] For cellulose, rising temperatures in HTC cause disruption of the fibrous network, forming nano- to microsized fragments that adopt rounded morphologies to minimize their interfacial energy with arene motifs as a dominant structure type. Dissolved glucose forms HTC spheres of 100–200 nm diameter that grow with residence time until reaching a size determined by the processing temperature. At temperatures above 200 °C and with longer residence times, the polyfuranic chains characteristic of glucose-derived HTC carbon at 180 °C undergo intramolecular condensation, dehydration, and decarboxylation, yielding more con-

densed sp^2-hybridized aromatic species analyzed by Falco *et al.* using XRD and ^{13}C-solid state NMR.[64] Non-reducing carbohydrates such as starch and amylopectin, unlike cellulose, produce furan-rich HTC carbon because their less ordered polysaccharide structures hydrolyze more readily at lower temperatures (<180 °C),[76,77] which is in line with the early release of sugars into the filtrate observed in this study from starch-rich WCGF. Crystalline cellulose conversion proceeds mainly through a pyrolysis-like pathway, with the polymerization of dissolved intermediates playing a secondary role. Knežević *et al.* could observe the formation of repolymerized char as a dominant route for cellulose only at higher HTC temperatures (~350 °C), due to enhanced cellulose dissolution at this temperature.[77]

Hydrochar and pyrolyzed carbon characterization

For the pH-dependent analysis of hydrochar and its annealed carbon products, a reaction temperature of 240 °C was selected. At this temperature, the HMF concentration dropped below 3% for wheat straw and was completely depleted for WCGF at an initial pH of 7. Moreover, previous studies have shown that carbon products formed above this temperature exhibit a higher degree of aromatization.[75] Elemental analysis further confirmed that the solid products obtained at 240 °C contained the lowest oxygen content, which is crucial for producing high-carbon amorphous materials after subsequent pyrolysis of hydrochar. The pyrolysis reaction can best be followed by thermogravimetric analysis coupled with mass spectrometry (TG-MS). The temperature program used can be found in the Materials and methods part in the SI. Briefly, 5 mg of the sample was heated to 100 °C for 15 min, before the temperature program (100–1000 °C, 10 K min^{-1}, He) was employed. In Fig. 4a, the relative TG and derivative TG curves of HTC treated WCGF and wheat straw and untreated biomass can be seen. The residual mass of the untreated samples after removal of water is 10 wt% for WCGF and 13 wt% for wheat straw, whereas the HTC-treated samples expectedly have a reduced mass loss due to the condensed furan and aromatic structures formed during the pretreatment. Note that the pH_{start} 0 treated samples exhibit the highest residual masses of around 42–45 wt% in both cases, which is similar to the sucrose model system (46 wt%, Fig. S23). In untreated WCGF, four major pyrolysis zones are distinguishable. The first mass loss begins at 150 °C, likely from hemicellulose or less ordered carbohydrates such as starch. The second step, peaking at 300 °C, could originate from hemicellulose and holocellulose, decomposing *via* side-chain dissociation, glycosidic bond cleavage, and subsequent ring-opening, dehydration, and decarboxylation, producing CO, CO_2, and other volatiles.[78] The third step at 350 °C corresponds to cellulose charring, while the fourth peak at 410 °C aligns with lignin decomposition. Lignin decomposes over 200–700 °C through ether bond cleavage, demethoxylation, and demethylation, releasing phenolics, guaiacols, catechols, and benzene derivatives, overlapping

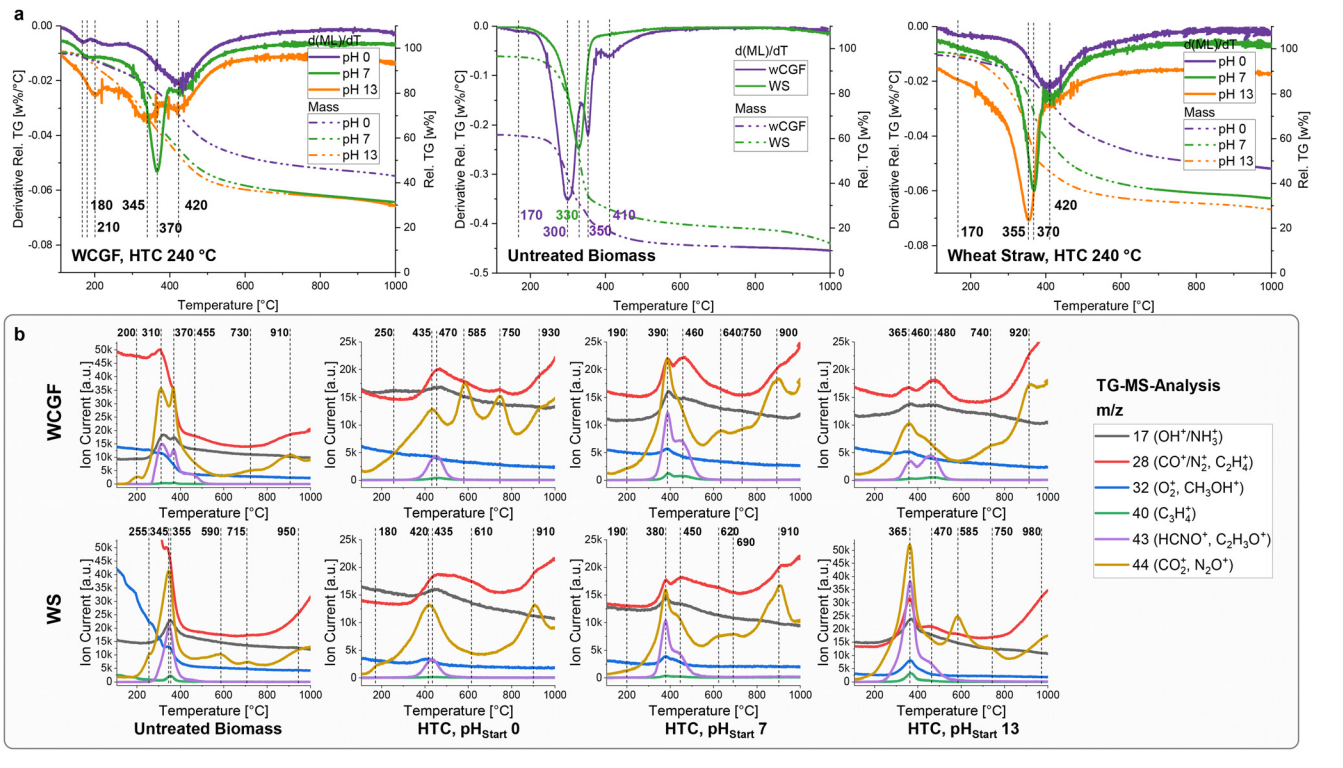

Fig. 4 TG-MS analysis in He gas of untreated biomass and HTC-treated biomass at 240 °C for 12 h at different starting pH values. All depicted curves were measured after a 1 h drying step to remove water. (a) Mass and derived mass loss curves with reaction steps marked at the measured sample temperature. (b) Temperature-dependent MS analysis of specific pyrolysis gas molecules.

with secondary char formation.[79,80] In the wheat straw DTG curve, only one step is visible, but MS signals show the main loss peak at 345 °C with a 255 °C shoulder, indicating an overlap of cellulose and less ordered carbohydrates. Proteins and lipids decompose over the ranges of 250–600 °C and 300–500 °C, respectively,[81] overlapping with secondary cracking of tar and bio-oil vapors at 550–900 °C, which produce H_2, CH_4, CO, CO_2, and polycyclic aromatic hydrocarbons, increasing carbonization of the solid residue.[79]

Varying the starting pH in HTC-treated biomass produces consistent DTG trends: low pH shifts maxima to higher temperatures, while high pH shifts them to lower temperatures. In sucrose and biomass hydrochars, the earliest DTG maximum (170–210 °C) is likely due to small, weakly polymerized HTC fractions. The 40 *m*/*z* ($C_2H_3^+$) signal is associated with the decomposition of furanic and low-ordered aromatic structures,[82] formed either during HTC pretreatment or *in situ* pyrolysis. In pH_{start} 7 samples, the main peak at 370 °C (MS 380–390 °C) could correspond to the decomposition of condensed HTC-secondary char units, followed by a 420 °C event that may arise from condensed aromatic and furanic structures originating from cellulose, lignin, or the HTC core. The sucrose model system (Fig. S23; HTC, 240 °C, pH_{start} 7, 12 h) shows a broad DTG peak at 385 °C, with $C_2H_3^+$ and $C_2H_3O^+$ loss peaking at 226 °C and CO^+ loss extending to 600 °C, similar to HTC-treated biomass. However, heavy overlap of reactions makes TG-MS deconvolution ambiguous. pH_{start} 0 biomass notably lacks the 370 °C peak, showing only the 420 °C event, suggesting the formation of a more carbonized HTC material. WCGF additionally exhibits 44 *m*/*z* (CO_2^+ and/or N_2O^+) events at 585 and 750 °C, possibly linked to N-functionalization, which are absent in sucrose. High-pH samples show maxima at 345–355 °C, close to native cellulose decomposition. Secondary charring above 800 °C appears more pronounced in HTC-treated biomass and sucrose, whereas untreated biomass primarily decomposes between 200 and 450 °C. HTC prestructuring facilitates aromatization into high-carbon char, as evident from elemental analysis and XRF of the amorphous chars (Fig. S19, S21 and S22). For the synthesis of the amorphous carbons, typically, 2 g of the sample was annealed at 1000 °C under Ar (5 K min^{-1}, 4 h) after repeated evacuation and Ar purging. The oxygen content of directly annealed biomass was 8 wt% for WCGF and 19 wt% for wheat straw, whereas HTC-treated samples decreased to 2 wt% for both. The highest char yields were obtained for pH_{start} 0 samples as indicated by the TG-MS mass loss. For wheat straw, HTC also appears to retain nitrogen species in the char, likely due to protein-derived aromatic compounds formed *via* Maillard reactions with available sugars in aqueous media.

To investigate the structural differences of the biomass-derived amorphous carbons, X-ray photoelectron spectroscopy (XPS), X-ray diffraction (XRD), scanning electron microscopy (SEM), Raman spectroscopy, N_2-sorption with Brunauer–Emmett–Teller (BET) and t-plot analysis and pressure-dependent bulk conductivity measurements were performed. A summary of selected results is shown in Fig. 5, with detailed measurement conditions provided in the Materials and methods in the SI. XPS, with an information depth of *ca.* 5–10 nm, probes chemical groups in the surface layers.[83] The C 1s KLL-edge, an Auger process providing information on the local bonding environment, can be fitted to estimate the sp^2/sp^3-bonding ratio. The so-called *D*-parameter is 13.5 eV for an sp^3-carbon reference (*e.g.*, low-density polyethylene) and 22.1 eV for an sp^2-carbon reference (*e.g.*, graphite) (Fig. S25).[84] Raman spectroscopy, based on inelastic scattering of light (532 nm), is used to evaluate the amorphous or graphitic state of the bulk with a probing depth that depends on the adsorption/scattering of carbon but can be estimated to be 0.1–10 μm.[85] The I_D/I_G ratio indicates amorphous-to-graphitic transition, with all studied materials classified as stage II amorphous carbons, with similar peak widths and positions.[39]

Powder conductivity was measured using a four-electrode in-house cell developed at the Hydrogen and Fuel Cell Center (ZBT GmbH), where the sample was compressed in 10 N cm^{-2} steps from 10 to 130 N cm^{-2} using a pneumatic cylinder. Conductivity is critical for minimizing ohmic losses in fuel cell catalytic layers. Increasing compression improves interparticle contact, enhancing bulk conductivity through delocalized π-bonds in sp^2-carbons.[86] The conductivity and derived particle density is compared in Fig. 5a, with values reported at 100 N cm^{-2}, corresponding to the compression force applied in fuel cells at ZBT GmbH.[48] Full pressure-dependent data are provided in Fig. S32.

The SEM images in Fig. 5a reveal pronounced morphological differences in HTC-treated samples depending on the starting pH.

Spherical particle formation is most evident in pH_{start} 0 samples and least in pH_{start} 13 samples, consistent with the NMR-based mechanistic analysis of filtrates. At higher pH, sugars and furfurals such as HMF follow alternative pathways yielding smaller organic acids and ketones, whereas low pH promotes levulinic acid formation from sugars and acid-catalyzed polymerization, resulting in hydrochar with a higher C content. In SEM micrographs of pyrolyzed sucrose hydrochar, HTC spheres are clearly visible (6–15 μm at pH_{start} 0, 2–10 μm at pH_{start} 7), with larger conjugated spheres at lower pH (Fig. S28); this is in line with previous observations by Reiche *et al.*, who observed a similar trend at a starting pH below 3 with sugar model systems.[87] By contrast, pH_{start} 13 favors larger carbon plates with fused spheres (Fig. S28c). Directly pyrolyzed biomass has a flake-structured morphology, and in wheat straw, remnants of cell wall pores are preserved. The spider charts of the pyrolyzed materials (1000 °C, 4 h, Ar, 5 K min^{-1}) can be interpreted, such that a larger enclosed area of the five connected parameters indicate more favorable properties for electrochemical applications. Directly pyrolyzed biomass shows comparatively low bulk conductivity and *D*-parameters that imply a lower content of sp^2-carbon. One could derive that the improved conductivity of HTC-treated biomass is primarily due to the higher sp^2-content; however, the WCGF and wheat straw data in the left and right spider

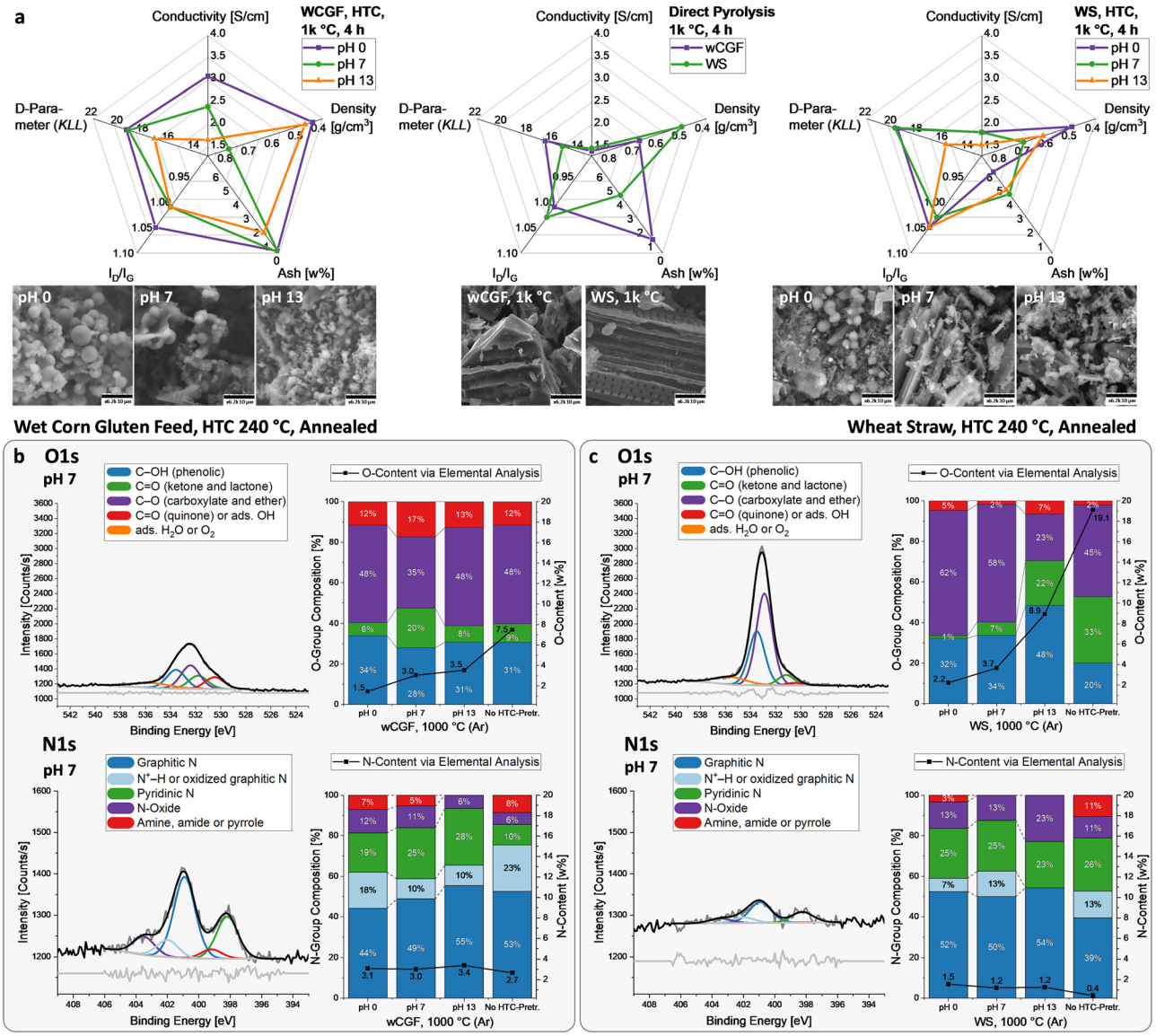

Fig. 5 Data of amorphous carbons with different HTC pretreatment conditions or no pretreatment, annealed at 1000 °C for 4 h in Ar gas. Errors of each method can be found in the SI and do not undermine the observed trends. (a) Spider chart comparing min./max. values of powder bulk conductivity [S cm^{-1}] and density [g cm^{-3}] measured at 100 N m^{-1} compression force and ash content from XRF analysis to the Vulcan XC72 reference material (see the SI). I_D/I_G ratio from Raman spectroscopy and *D*-parameter acquired from XPS analysis with min./max. values oriented on the sp^2/sp^3 reference material. Larger enclosed area of the five connected parameters indicates favorable properties for electrochemical applications. Spider chart, SEM images of the pyrolyzed carbons all with a 10 μm scale bar. O 1s and N 1s functional group analysis with exemplary XPS spectrum of the pH 7 sample and O- and N-weight content *via* elemental analysis of (b) WCGF-derived materials and (c) WS-derived materials.

chart show comparable hybridization and hence indicate that ash content and the degree of HTC-particle formation are also important factors influencing the conductivity. Since high density (*e.g.*, in the pH_{start} 7 samples) does not necessarily result in better conductivity—as might be expected from closer packing—it can be concluded that the chemical connectivity of carbon units has a more significant impact on bulk conductivity. The high-HTC-accessible-sugar containing WCGF forms connected HTC particles most effectively at low starting pH; in this sample, the conductivity is the best. The pH_{start} 7 samples exhibit less visible HTC-particle formation in the SEM micrographs and the reaction mechanisms are more similar to those of pH_{start} 13 samples, leading to a reduced conductivity in the case of WCGF. While a low starting pH leads to repolymerized HTC particle formation in wheat straw as well, the silicon retention is the highest in this sample, which might explain why the conductivities of pH_{start} 0 and 7 samples are virtually the same. The limited particle formation, as well as the higher ash content (mostly silicon) in the wheat straw, reduces the conductivity by 40% compared to the pH_{start} 0 WCGF sample. Additional desilication steps could involve alkali pretreatment[88] or extraction with a chelating agent such as sodium

citrate.[89] Vulcan XC72 as a commonly used petroleum-derived carbon with a morphology of connected and fused spherical particles in the 20–50 nm range (STEM image in Fig. 7a, C) exhibits a bulk conductivity of 3.9 S cm^{-1} at 100 N m^{-1}. This is 30% higher than the WCGF (pH_{start} 0), despite having comparable density, *D*-parameter, ash, and I_D/I_G values (Fig. S24a). The increased conductivity can again be explained by the better interparticle connectivity and more homogeneous arrangement of the carbon spheres. XRD analysis suggests that Vulcan XC72 also has a slightly better long-range graphitic ordering (Fig. 7b), which also leads to the improved conductivity compared to the WCGF-derived amorphous carbons. The implications of these trends can help assess early on which biomass precursors can be feasible for application in electrocatalysis and how the HTC-reaction conditions need to be improved depending on the biomass.

In the SEM images of the wheat straw, the original cell structure was preserved, being possibly the reason why a macroporous morphology is observed in N_2-sorption experiments (Fig. S31a; N_2-sorption isotherms). A high starting pH leads to alkaline hydrolysis of lignin monomers, increasing lignin solubility and breakdown; hence porosity is lost and the surface area determined by BET analysis is decreased for wheat straw treated under these starting conditions. Vulcan XC72 has a surface area in the same order of magnitude as the wheat straw materials (Table 2), but the N_2-sorption curves imply micropore content, which was estimated to be 75.6 m^2 g^{-1} using a t-plot analysis (Fig. S37b). The biomass-derived samples exhibit an isotherm type III sorption behavior and therefore could not be analyzed by t-plot analysis due too little or no micropore volume, hence resulting in a negative intersection with the *y*-axis. For the directly pyrolyzed WCGF samples, no surface area could be determined because the *C* values were unsuitable, likely due to weak N_2-surface interactions combined with the inherently low surface area of the material. Sugar-derived HTC-treated carbons depending on the reaction conditions can give a high surface area with micro- and mesopores,[90] but it has been previously observed by our group that the addition of nitrogen into the HTC-carbon matrix seems to lead to a smoother surface with no micropores, large macropore content and low specific surface area.[91] Consequently, the annealed HTC-treated WCGF with N-contents around 3 wt% also shows no micropores and a low surface area. Another reason for the difference in the surface area between wheat straw and WCGF could be that WCGF does not exhibit a high lignin content that keeps the cell wall structure in place, either during HTC treatment or during direct annealing. As previously observed by other groups, the surface area determined by the BET method does not seem to correlate with the bulk conductivity.[48]

To estimate the accuracy of the XPS fitting, the atomic concentration of each N and O component was summarized and divided by the sum of carbon–heteroatom bonds fitted into the C 1s peak (O 1s + N 1s/C 1s–heteroatom). The ratio of this quality indicator should be 1 ± 0.1. High heteroatom contents can lead to a large error in the C 1s peak fitting and underestimation of total O and N contents, which is why for the CNO composition, elemental analysis combined with XRF is the most reliable method for some of the samples.[92–94] The O and N content shown in Fig. 5b, c was measured by elemental analysis. The XPS analysis shows that during pyrolysis, N-functional groups (amine, amide or pyrrole and NR_3-nongraphitic groups) aromatize to pyridinic and graphitic nitrogen (Fig. S26, O 1s and N 1s of hydrochar). Due to the high oxygen contents in the hydrochar, nitrogen containing groups can be oxidized to *N*-oxides, even under an inert Ar atmosphere. In pyrolyzed WCGF, the composition of the oxygen groups does not change significantly; however, their amount doubles if the biomass is not HTC-treated. For wheat straw, the phenolic and ketone or lactone content is increased at pH_{start} 13, possibly because of a more exposed and broken lignin scaffold. This is also indicated by an increased amount of carboxylate or ether groups in the unannealed hydrochar (Fig. S26b), which, in the case for ether can cleave and yield phenolic groups on the surface layers of the carbon. Exposed lignin moieties may form an oxygen-rich scaffold, leading to a high residual oxygen content. The HTC-treated biomass samples with low starting pH have similar oxygen content to Vulcan XC72 (1–2 wt%) but also primarily contain sp^2-bound nitrogen in their carbon matrix. Basic nitrogen surface groups like amine, amide and pyridinic groups or positively charged N-groups will increase the ability to interact with negatively charged ions in the functional groups of a Nafion ionomer, which is mixed with the conductive carbon for catalyst ink formulation.[50,51]

The effects on the formation mechanism of hydrochar and amorphous carbon derived from biomass are summarized in Fig. 6. It illustrates why HTC-pretreatment can help improve the interparticle connectivity and purity of the materials triggered by reaction mechanisms in the liquid phase described in Fig. 3c and the previous sections. Depending on the original components that make up the biomass, hydrolyzable fractions and alkali metals are dissolved into the HTC filtrate.

Table 2 BET and t-plot analysis data of biomass-derived materials against commercial carbons

Pyrolyzed materials	HTC (240 °C, 12 h)	Surface area [m^2 g^{-1}]	*C*	Micropore & external surface area [m^2 g^{-1}]
WCGF	pH 0	33	4.8	0
	pH 7	28	6.3	0
	pH 13	24	3.1	0
	None	—	—	—
Wheat straw	pH 0	220	9.7	0
	pH 7	188	5.4	0
	pH 13	22	4.1	0
	None	227	3.2	0
Vulcan XC72	—	298	125.2	76, 222
Mesoporous carbon	—	145	13.5	0

All correlation coefficients >0.99. The pH refers to the starting pH.

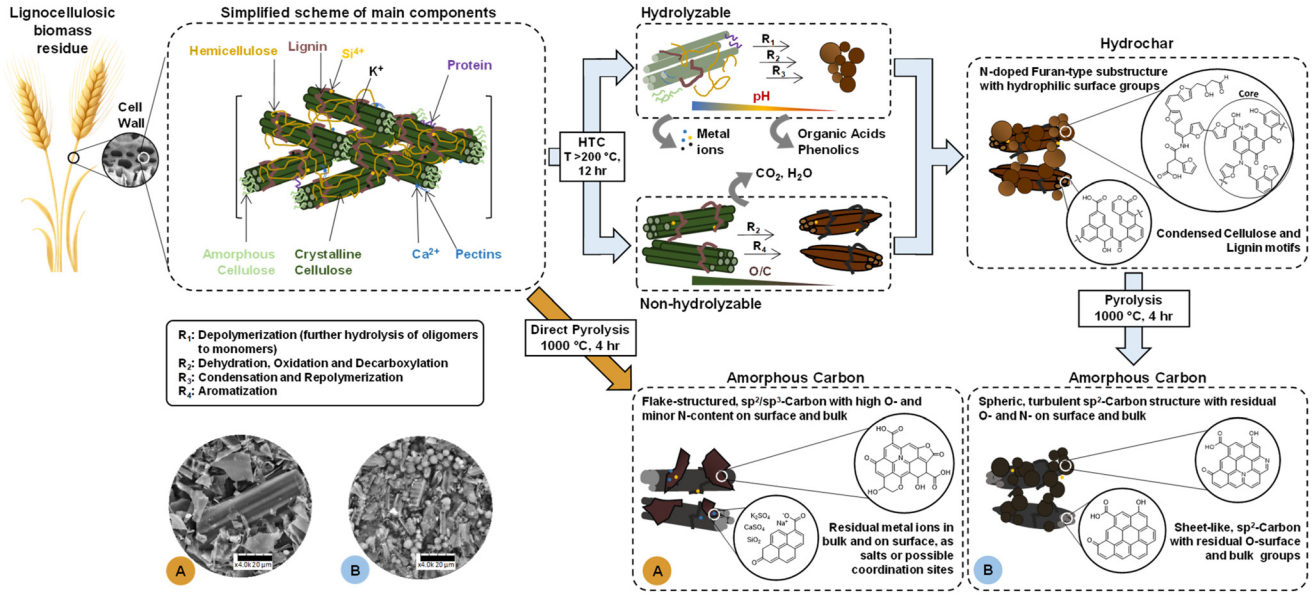

Fig. 6 Illustration of the decomposition pathways of simplified lignocellulosic biomass components under hydrothermal conditions leading to hydrochar formation, with structural comparison to direct pyrolysis.

Compared to the sugar model system, the accessibility and exposure of the biomass components are limited by hydrophobic units like lignin or highly crystalline cellulose that only partly decompose starting at 220 °C and undergo mostly solid–solid transformations.[76] Its fibrous network starts to get disrupted, leading to the formation of nano/micro-sized cellulose fragments, which, being insoluble in water, adopt rounded shapes to minimize their contacting interface with the surrounding aqueous environment.[64] Sugars, phenolics and proteins will undergo dehydration, oxidation and decarboxylation reactions that lead to intermediates like furfural and HMF, which readily polymerize into spherical particles. Furfural stemming from C5-sugars is more likely to undergo Strecker degradation with amino acids like glycine to form 3-hydroxypyridine derivatives compared to C6-sugars which tend to degrade *via* different mechanisms leading to levulinic acid and smaller C3 & C4 ketones and acids. This leads to a hydrochar with higher N-content in the case of C6-sugar as the carbon source. Amino acids and phenolics from lignin or hemicellulose can repolymerize as well and lead to N-containing hydrochar. Lowering the starting pH can improve the hydrolysis to form monomers that can polymerize to HTC particles, since in biomass the concentration of available degrading sugar in solution is never high enough to reach the level of autocatalysis of non-buffered sucrose solution during HTC (rapid pH-drop due to formed acids). The sugar-derived HTC particles were shown to have a core–shell type of morphology.[19] It has been proposed that core growth is driven by dehydration reactions forming β-linked furanic domains and arene clusters, while surface functionalities arise from pathways involving aqueous HMF, likely through aldol condensation or catalyzed ring-opening reactions.[20] When hydrochar is annealed, the previously formed furan-based structures can form a turbostratic carbon type that maintains its spherical structure. These interlinked particles formed on top of carbon sheets that stem from the non-hydrolyzable part of the biomass, which undergoes mostly solid–solid transformations, help to improve the bulk conductivity and homogeneity of the material. Secondary charring reactions above 800 °C are more pronounced in the MS traces of HTC-treated biomass and the sucrose model system than in untreated biomass. While untreated biomass primarily loses carbon through the release of volatiles at low temperatures (200–450 °C), HTC pretreatment introduces structural rearrangements that promote aromatization and the formation of carbon-rich char. This pathway also governs bulk electrical conductivity through four coupled levers: (i) a higher sp^2/sp^3 ratio from furan-to-aromatic conversion lowers electronic transport barriers; (ii) HTC-driven formation and coalescence of interconnected spheres improve particle–particle contact and percolation; (iii) nitrogen retained from protein-rich feeds introduces possible defect sites that could facilitate charge transport;[95] and (iv) minimization of inorganic residue, especially silica, prevents insulating phases that interrupt current paths. The directly pyrolyzed biomass material has a lower sp^2/sp^3-ratio, higher alkali metal contamination and less interconnected particles, which lead to lower conductivity.

Pyrolyzed hydrochar as a support in electrocatalysis

As a proof of concept, the most promising biomass-derived chars and Vulcan XC72 were decorated with Pt nanoparticles (NP) *via* the chemical deposition method adopted by Fang *et al.*[96] and compared to a commercial Pt (40 wt%) on the carbon catalyst (Sigma-Aldrich). The catalysts were analyzed by scanning transmission electron microscopy (STEM), XRD, and XRF, and electrochemically assessed at room temperature

(22 °C) on a Metrohm RDE setup. The Pt NP distribution and average diameter calculated from the manual particle count from STEM images are shown in Fig. 7a. The adopted chemical deposition method yielded a slightly smaller particle size (2 to 2.3 nm) on the biobased carbons than the commercial catalyst (2.7 ± 0.1 nm), with comparably narrow distributions, making the catalysts good candidates for electrochemical application. When the broad diffraction peaks of Pt in XRD patterns are fitted, similar sizes, within the margin of error, are observed (Fig. 7b and Fig. S30, Pt fcc fitting). Differences arise from the distinct methodologies employed: the XRD-derived particle diameters are obtained as volumetric mean values of crystallites, while the STEM evaluation gives an arithmetic mean of a selected number of particles. Reduced particle size can improve the dispersion of Pt on the support material and maximizes the surface-to-volume ratio.[97] The chosen biomass-derived carbons provide functional surface groups that enable well-distributed Pt NPs. Carbon corrosion testing was not done on the RDE due to the limited insight it gives on actual fuel cell operation; in a fuel cell, the catalyst experiences gas-phase oxygen, variable humidity, and complex mass transport limitations, leading to significantly different local potentials and corrosion dynamics.[54] What carefully employed RDE measurements can bring are the comparison of intrinsic kinetic parameters and activities.[98] To compare the availability of Pt NP on different carbon supports, their electrochemically active surface area (ECSA [$m^2\ g_{Pt}^{-1}$]), mass-specific current (I_m [$A\ g_{Pt}^{-1}$]), area-specific current (I_S [$\mu A\ cm_{Pt}^{-2}$]) and kinetic Tafel slope value [$mV\ dec^{-1}$] were acquired and compared, as shown in Fig. 7d. Measurements were performed in a three-electrode glass cell with a leak-free reference Ag/AgCl electrode separated from the main compartment with an electrolyte bridge in 0.1 M $HClO_4$ solution. The washing procedure of glassware and the adopted electrochemical protocol along with the equations used can be found in the work of Shinozaki *et al.*[55] To check the cleanliness of the electrochemical setup, the area-specific current at 0.9 V *vs.* RHE of a polycrystalline Pt RDE in O_2-purged electrolyte solution should be between 1.5 and 3 mA cm^{-2}.[98] The value in this setup was 2.2 mA cm^{-2} (Fig. S36a, 20 mV s^{-1}, 1600 rpm, anodic sweep). A stock solution of 24 mL isopropanol, 76 mL ultrapure water and 0.4 mL of 5 wt% Nafion solution (Ion Power, 1100 EW) was made for the commercial and the Vulcan XC72 catalyst. For the usual ink formulation, 3.5 mg of catalyst was mixed in a 10 mL stock solution. Since previous studies showed that high sonication intensities and long exposure times can lead to a change in

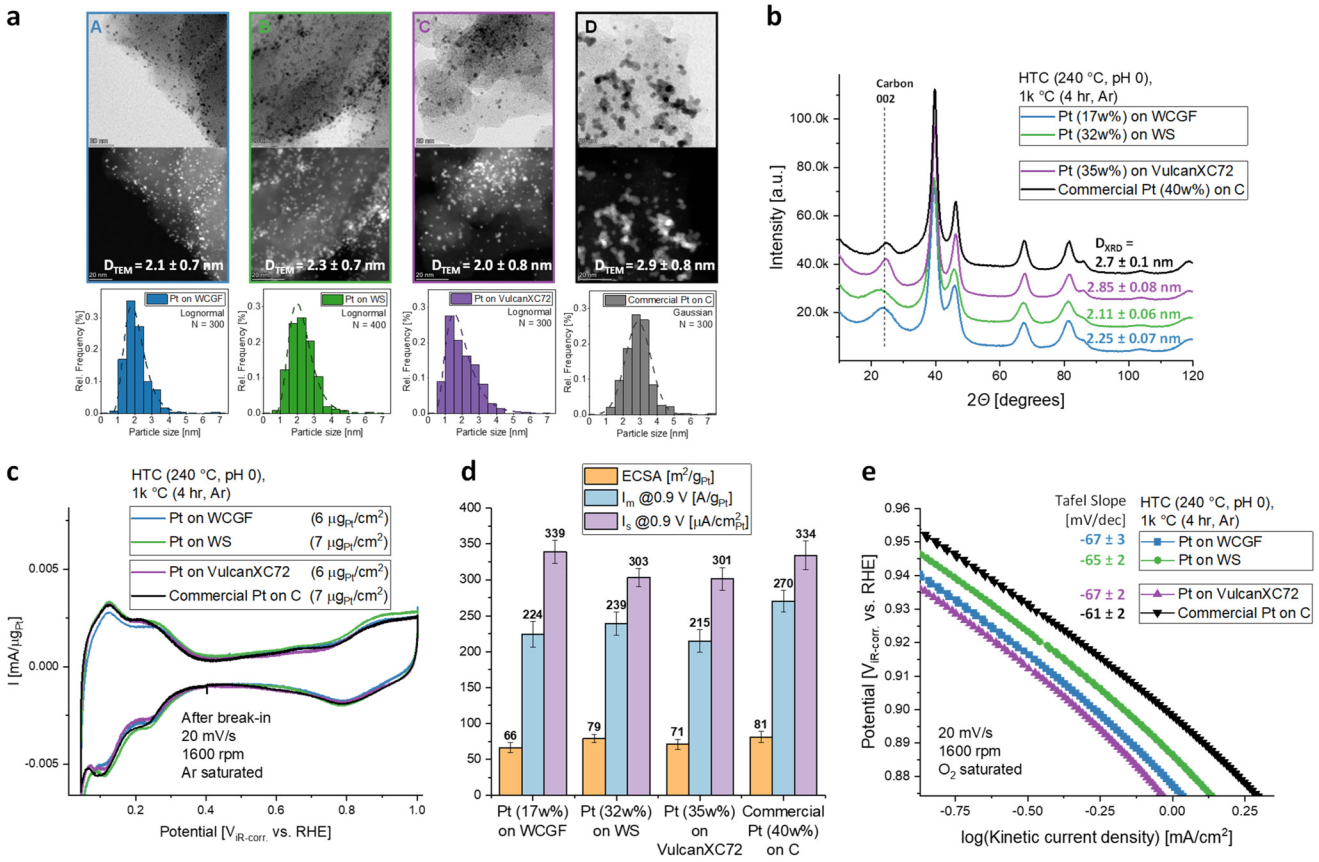

Fig. 7 All electrochemical experiments were done at 22 °C. (a) STEM bright and dark field images of WCGF (A), WS (B), Vulcan XC72 (C) and commercial Pt on carbon (D) catalysts with particle distributions and average particle size. (b) XRD diffractogram of catalysts and average particle size from Pt fcc fitting. (c) *iR*-Corrected CV spectra plotted in mA μg_{Pt}^{-1} for comparable peak heights of different catalysts. (d) Bar graph of ECSA, background current-corrected kinetic and mass currents of the ORR at 0.9 V *vs.* RHE. (e) Tafel slope of ORR currents in the kinetic regime.

surface chemistry of the catalyst,[99] a short sonication time of 6 min in a temperature-controlled ice bath was employed. It is well known that the drop casting of the ink on the glassy carbon surface of the RDE is a large source of error (coffee ring and inhomogeneous film formation).[100] To get an error estimation and mean value, drop casting of a 10 μL droplet on a 5 mm glassy carbon disk was done twice *via* the rotational drying method[101] and once with air drying in a ventilated oven at 40 °C while covering the RDE tip with a glass beaker for slow drying for 40 min. The cyclic voltammetry (CV) curves in Fig. 7c, from which the ECSA was deducted *via* integration of H-UPD (hydrogen-underpotential deposition) peaks, are measured after preconditioning the 100 cycles in Ar purged solution in a potential window of 0–1.4 V *vs.* RHE (Fig. S34a, CVs before break-in, Fig. S34b, CVs of conditioning). 210 μC cm_{Pt}^{-2} was used for ECSA calculation as the conversion factor, *i.e.*, the canonical charge for a monolayer of hydrogen adsorbed on polycrystalline Pt in acid.[102] The catalysts that had a higher surface area determined by the BET method also exhibit a slightly higher ECSA, though lying within each other's error bars; the low surface area WCGF, with a lower loading of Pt (17 wt%) to avoid clustering, has a mean ECSA of 66 m^2 g_{Pt}^{-1}, whereas the macroporous wheat straw-derived catalyst and the commercial catalyst exhibit an ECSA of around 80 m^2 g_{Pt}^{-1}. The N_2-sorption notably does not linearly correlate to the ECSA of Pt, since the availability of Pt in the electrocatalysts depends on many other factors like NP size, homogeneous distribution on the carbon surface and interaction of the Pt NP on the carbon surface. Gas diffusion through the carbon matrix has a large impact on the CL in a fuel cell and cannot be properly assessed with the RDE. Studies have shown that supports with low micro- and macropore surface areas determined by the BET method, dominated by mesoporous morphology, yield catalyst layers with enhanced ORR kinetics and reduced local O_2- and bulk H^+-transport resistances.[47] The biggest difference in electrochemical performance between the commercial catalyst and the ones synthesized in this study is found in the mass-specific current I_m, where the commercial catalyst outperforms by 30 A g_{Pt}^{-1} compared to the wheat straw-derived catalyst. This jump can come from the different deposition methods of the Pt NPs, where clustering can lead to less effective usage of mass per catalyst unit. Evidently, other effects like particle detachment and transient dissolution, which can be countered by strong anchoring of the NP to the carbon surface, can also lead to a loss of mass activity.[103] Carefully designed Pt deposition methods have been shown to improve mass specific activity, which was not the incentive in the scope of this study. The specific kinetic activity I_S is the highest in the WCGF-derived and the commercial catalyst. Catalysts may exhibit lower kinetic currents when their intrinsic activity is reduced due to unfavorable binding energies of oxygen intermediates, or when the effective utilization of active sites is limited by factors such as large particle size, poor dispersion, low-conductivity supports, or surface poisoning, which could be the case for the wheat straw catalyst since residual silicon and lower conductivity were measured. As analyzed thoroughly with microkinetic modeling and single crystal Pt electrodes, a Tafel slope close to −60 mV dec^{-1} at low overpotential can indicate that the initial electron transfer serves as the rate-determining step, with the rate being highly dependent on the coverage of platinum oxide groups and hence the pH and potential.[104,105] All of the analyzed catalysts are within the margin of error in this regime, with the commercial catalyst having the lowest average slope. Although thin films are complex systems, which make them unfit for detailed mechanistic analysis,[106] due to the chemical similarity of the compared catalysts (Pt on carbon), the results indicate analogous ORR pathways at the Pt surface.

STEM and XRD show that comparable Pt NP distributions and RDE performances to the synthesized Vulcan XC72 supported catalyst can be reached with biomass-derived carbons. While RDE results can give a good impression on the kinetics of a catalyst at the measured temperature, the stability and real performance in a fuel cell are on a different page. The performance measured with RDE often deviates from real fuel cell operation because the RDE provides idealized conditions with well-controlled mass transport and uniform reactant distribution, whereas practical fuel cells involve factors such as gas diffusion, water management, ionomer–catalyst interactions and electrode architecture that significantly influence catalytic activity and durability. For this reason, high surface area carbons (HSC) can be more desirable since the porous carbon network facilitates gas diffusion and reactant accessibility, which supports more efficient oxygen transport to catalytic sites. If the catalyst used in this study were to be compared to RDE activities of HSC catalysts of other reported studies, they would show similar ECSA in the case of the wheat straw derived catalyst, but mass-specific currents of HSC can be up to twice as high in a well-optimized ink formulation and RDE setups.[101] Several things can be learned for catalyst manufacturing from biomass-based materials by the comparison of parameters, as shown in Fig. 5a and the electrochemical testing. HTC-pretreated sugar- and protein-rich biomass (*e.g.*, wet corn gluten feed) can form N-doped amorphous carbons with excellent purities and increased bulk conductivity due to effective hydrolysis and repolymerization to interconnected spheres, but the resulting non-porous and low surface area determined by the BET method may lead to activity losses when a Pt-decorated catalyst is fabricated, where pore sizes play an important role. To improve the surface area, a subsequent chemical activation step with KOH[107] or physical activation with CO_2 could be considered.[108] Biomass with increased non-hydrolyzable contents like lignin and crystalline cellulose (*e.g.*, wheat straw) retain part of their cell-wall structure through solid–solid transformation during HTC, which leads to an increased surface area (by BET analysis), but decreased content of repolymerized and connected primary particles, meaning a loss in conductivity. Straw-type materials have the disadvantage of high silicon content which depletes significantly with HTC pretreatment but is still too high for applications that require pure carbon materials, making additional desilication pretreatments necessary. Understanding the for-

mation mechanisms of hydrochar for the subsequent pyrolysis is the first step to optimize biomass-based carbons towards efficiencies closer to petroleum-sourced carbon materials.

Conclusion

Comprehensive qualitative and quantitative analysis using 1D- and 2D-NMR highlights the need to analyze both hydrochar and filtrate in hydrothermal processes to understand the underlying chemistry of solid- and liquid-product formation. Identification of filtrate components enables the evaluation of potential platform chemicals (*e.g.*, levulinic acid, 3-hydroxypyridine, and furfurals) as well as considerations regarding toxicology and downstream processing. In the sugar model system of sucrose, acid-catalyzed formation of levulinic acid and repolymerized hydrochar from furfurals (mainly HMF) is already significant at pH_{start} 7, since dissolved sugars rapidly decompose to acids that lower the pH (at 200 °C after 6 h pH_{end} 3, after 12 h pH_{end} 2). The content contributions of the sugar model system only start to resemble those of biomass when a higher starting pH is used; here OH^- buffering slows down the pH reduction, as for the biomass (wheat straw and wet corn gluten feed), the concentration of available degrading sugar in solution is never high enough to reach the level of autocatalysis of non-buffered sucrose solution. This means that many other side reactions can occur, which lead to the formation of high amounts of C3 and C4 acids, ketones, aldehydes and alcohols that lower the yield of carbon-rich and oxygen-reduced hydrochar. NMR analysis revealed protonated 3-hydroxypyridine derivatives as the main N-containing molecule in both biomass filtrates, likely formed *via* Strecker degradation of a 1,2-diketone derived from a C5 sugar. The preference of C5 sugars *vs.* C6 sugar to undergo this degradative reaction with an amino acid was confirmed with model system reactions of glycine with D-xylose (C5 sugar) and D-glucose (C6 sugar). In biomass, a low starting pH resulted in a filtrate molecule content closer to the model system and in hydrochar with lower oxygen content and increased spherical HTC-particle formation. During the subsequent pyrolysis (1000 °C, 4 h, Ar), the hydrothermally formed furan-based structures promote aromatization and the formation of carbon-rich char. The non-HTC treated, directly pyrolyzed biomass has a lower sp^2/sp^3-ratio, higher alkali metal contamination and no interconnected particles, which reduces percolation and leads to a lower bulk conductivity. In summary, HTC-pretreated sugar- and protein-rich biomass such as wet corn gluten feed forms N-containing, amorphous carbons with high purity and enhanced conductivity through hydrolysis and repolymerization into interconnected spheres, although when used as a catalyst support for the ORR, the non-porous, low specific surface areas reduce catalytic activity, which could be resolved by an additional activation step. In contrast, lignocellulosic biomass like wheat straw retains parts of its cell-wall structure, yielding higher surface areas determined by the BET method but lower conductivity due to less HTC particle formation and ash contamination (mostly silicon). The high silicon content, although reduced by HTC, remains a limitation for applications requiring pure carbon materials, which is why an additional desilication step should be employed. These mechanistic outlines provide an idea for a material-selection map: use of sugar/protein-rich feeds when conductivity and purity are priorities (*e.g.*, electrodes and current collectors) and lignocellulosic feeds when surface area and high amounts of functional groups are necessary (*e.g.*, adsorbents and support materials), optionally followed by ash removal or secondary graphitization to rebalance the surface area–conductivity trade-off. With detailed insights into biomass formation pathways, we aim to advance the understanding of bio-based carbons and platform chemicals, driving the shift toward sustainable and efficient technologies.

Conflicts of interest

There are no conflicts to declare.

Data availability

The data supporting this article have been included as part of the supplementary information (SI). Supplementary information is available. See DOI: https://doi.org/10.1039/d6gc00237d.

Acknowledgements

The authors thank Marius Heise-Podleska (Max Planck Institute for Chemical Energy Conversion) for recording TG-MS data and for advice on measurement settings. Sebastian Tigges is thanked for his support with XPS analysis and Lukas Schubert for help with NMR data acquisition (Max Planck Institute for Chemical Energy Conversion). John-Tommes Krzeslack and Alin Benice Schöne are thanked for performing the XPS and STEM measurements (respectively, Max Planck Institute for Chemical Energy Conversion). The authors also thank the Instrumental Analytics Group of Justus Werkmeister (Max Planck Institute for Chemical Energy Conversion) for performing elemental analysis and XRF measurements. The authors thank Ioannis Spanos, Aleksandar Zeradanin, and Justus Masa (Max Planck Institute for Chemical Energy Conversion) for providing electrochemical equipment for RDE measurements. The authors further thank Thomas Lange (Hydrogen and Fuel Cell Center, ZBT GmbH) for providing data analysis tools for bulk conductivity measurements, and TerraNova Energy GmbH for providing wet corn gluten feed as a biomass precursor. Open Access funding provided by the Max Planck Society.

References

1 J. Zhang, J. Gu, R. Shan, H. Yuan and Y. Chen, *Resour., Conserv. Recycl.*, 2025, **212**, 107905.

2 B. Zhang, B. K. Biswal, J. Zhang and R. Balasubramanian, *Chem. Rev.*, 2023, **123**, 7193–7294.
3 T. Kan, V. Strezov and T. J. Evans, *Renewable Sustainable Energy Rev.*, 2016, **57**, 1126–1140.
4 R. Sankaran, R. A. Parra Cruz, H. Pakalapati, P. L. Show, T. C. Ling, W.-H. Chen and Y. Tao, *Bioresour. Technol.*, 2020, **298**, 122476.
5 TerraNova Energy GmbH (Germany), https://www.terra-nova-energy.com/en/, (accessed 20.09.2025).
6 C-Green Technology AB (Sweden/Finland), https://www.c-green.se/, (accessed 20.09.2025).
7 SoMax BioEnergy (USA), https://somaxhtc.com/, (accessed 20.09.2025).
8 Ingelia (Spain), https://www.ingelia.com/en, (accessed 20.09.2025).
9 A. L. Pauline and K. Joseph, *Fuel*, 2020, **279**, 118472.
10 E. Berl and A. Schmidt, *Liebigs Ann. Chem.*, 1932, **493**, 97–123.
11 J. A. Libra, K. S. Ro, C. Kammann, A. Funke, N. D. Berge, Y. Neubauer, M.-M. Titirici, C. Fühner, O. Bens, J. Kern and K.-H. Emmerich, *Biofuels*, 2011, **2**, 71–106.
12 A. T. Fleck, F. T. McCollum, K. S. Lusby, F. N. Owens, D. S. Buchanan, H. W. Essig and W. M. Larson, *The Professional Animal Scientist*, 1988, **4**, 17–23.
13 T. Tufail, F. Saeed, M. Imran, M. U. Arshad, F. M. Anjum, M. Afzaal, H. Bader Ul Ain, M. Shahbaz, T. A. Gondal and S. Hussain, *Int. J. Food Prop.*, 2018, **21**, 1303–1310.
14 D. W. Templeton, E. J. Wolfrum, J. H. Yen and K. E. Sharpless, *BioEnergy Res.*, 2016, **9**, 303–314.
15 J. M. Kelzer, P. J. Kononoff, L. O. Tedeschi, T. C. Jenkins, K. Karges and M. L. Gibson, *J. Dairy Sci.*, 2010, **93**, 2803–2815.
16 F. Ahmad, T. R. K. C. Doddapaneni, S. S. Toor and T. Kikas, *Biomass*, 2025, **5**, 9.
17 D. Jung, M. Zimmermann and A. Kruse, *ACS Sustainable Chem. Eng.*, 2018, **6**, 13877–13887.
18 M.-M. Titirici, M. Antonietti and N. Baccile, *Green Chem.*, 2008, **10**, 1204–1212.
19 M. Sevilla and A. B. Fuertes, *Chem. – Eur. J.*, 2009, **15**, 4195–4203.
20 L. J. R. Higgins, A. P. Brown, J. P. Harrington, A. B. Ross, B. Kaulich and B. Mishra, *Carbon*, 2020, **161**, 423–431.
21 M. T. Reza, B. Wirth, U. Lüder and M. Werner, *Bioresour. Technol.*, 2014, **169**, 352–361.
22 G. C. Hayes and C. R. Becer, *Polym. Chem.*, 2020, **11**, 4068–4077.
23 C. Chen, M. Lv, H. Hu, L. Huai, B. Zhu, S. Fan, Q. Wang and J. Zhang, *Adv. Mater.*, 2024, **36**, 2311464.
24 J.-P. Lange, E. van der Heide, J. van Buijtenen and R. Price, *ChemSusChem*, 2012, **5**, 150–166.
25 N. Frank, M. Leutzsch and B. List, *J. Am. Chem. Soc.*, 2025, **147**, 7932–7938.
26 D. J. Burinsky and F. Wang, in *Separation Science and Technology*, ed. S. Ahuja and K. M. Alsante, Academic Press, 2004, vol. 5, pp. 249–299.
27 A. Kajtazi, G. Russo, K. Wicht, H. Eghbali and F. Lynen, *Chemosphere*, 2023, **337**, 139361.
28 C. N. McEwen and R. G. McKay, *J. Am. Soc. Mass Spectrom.*, 2005, **16**, 1730–1738.
29 F. Yue, C. M. Pedersen, X. Yan, Y. Liu, D. Xiang, C. Ning, Y. Wang and Y. Qiao, *Green Energy Environ.*, 2018, **3**, 163–171.
30 S. Ghoreishi, C. Løhre, D. H. Hermundsgård, J. L. Molnes, M. Tanase-Opedal, R. Brusletto and T. Barth, *Biomass Convers. Biorefin.*, 2024, **14**, 3331–3349.
31 H. V. Halleraker and T. Barth, *J. Anal. Appl. Pyrolysis*, 2020, **151**, 104919.
32 Q. Wu, L. Huang, S. Yu, S. Liu, C. Xie and A. J. Ragauskas, *ACS Sustainable Chem. Eng.*, 2017, **5**, 6131–6138.
33 G. Ischia, M. Cutillo, G. Guella, N. Bazzanella, M. Cazzanelli, M. Orlandi, A. Miotello and L. Fiori, *Chem. Eng. J.*, 2022, **449**, 137827.
34 P. Körner, *ChemSusChem*, 2021, **14**, 4947–4957.
35 W. Dominik, A. Pablo, H. Sonja, C. Fernando, F. Luca and K. Andrea, *Waste Biomass Valorization*, 2022, **13**, 2349–2373.
36 S. I. Kawamura, in *The Maillard Reaction in Foods and Nutrition*, American Chemical Society, 1983, vol. 215, ch. 1, pp. 3–18.
37 M. N. Mahmood Al-Nuaimy, N. Azizi, Y. Nural and E. J. E. r. Yabalak, *Environ. Res.*, 2023, 117923.
38 M. M. Titirici, A. Thomas, S.-H. Yu, J.-O. Müller and M. Antonietti, *Chem. Mater.*, 2007, **19**, 4205–4212.
39 D. B. Schuepfer, F. Badaczewski, J. M. Guerra-Castro, D. M. Hofmann, C. Heiliger, B. Smarsly and P. J. Klar, *Carbon*, 2020, **161**, 359–372.
40 E. Stefanelli, S. Vitolo, N. Di Fidio and M. Puccini, *J. Environ. Manage.*, 2023, **345**, 118887.
41 Q. Wang, H. Li, L. Chen and X. Huang, *Carbon*, 2001, **39**, 2211–2214.
42 Y.-S. Hu, R. Demir-Cakan, M.-M. Titirici, J.-O. Müller, R. Schlögl, M. Antonietti and J. Maier, *Angew. Chem., Int. Ed.*, 2008, **47**, 1645–1649.
43 M. Song, Y. Zhou, X. Ren, J. Wan, Y. Du, G. Wu and F. Ma, *J. Colloid Interface Sci.*, 2019, **535**, 276–286.
44 M. Borghei, J. Lehtonen, L. Liu and O. J. Rojas, *Adv. Mater.*, 2018, **30**, 1703691.
45 C. Durante, *Curr. Opin. Electrochem.*, 2022, **36**, 101119.
46 J. W. Straten, P. Schleker, M. Krasowska, E. Veroutis, J. Granwehr, A. A. Auer, W. Hetaba, S. Becker, R. Schlögl and S. Heumann, *Chem. – Eur. J.*, 2018, **24**, 12298–12317.
47 H. Iden, T. Mashio and A. Ohma, *J. Electroanal. Chem.*, 2013, **708**, 87–94.
48 A. S. Amin, A. Caidi, T. Lange, I. Radev, D. J. S. Sandbeck, W. Philippi, M.-A. Kräenbring, M. Öztürk, V. Peinecke, D. Lerche, F. Özcan and D. Segets, *Part. Part. Syst. Charact.*, 2025, **42**, 2400069.
49 S. Ott, A. Orfanidi, H. Schmies, B. Anke, H. N. Nong, J. Hübner, U. Gernert, M. Gliech, M. Lerch and P. Strasser, *Nat. Mater.*, 2020, **19**, 77–85.
50 W. Yoshimune, N. Kikkawa, H. Yoneyama, N. Takahashi, S. Minami, Y. Akimoto, T. Mitsuoka, H. Kawaura, M. Harada, N. L. Yamada and H. Aoki, *ACS Appl. Mater. Interfaces*, 2022, **14**, 53744–53754.

51 A. Orfanidi, P. Madkikar, H. A. El-Sayed, G. S. Harzer, T. Kratky and H. A. Gasteiger, *J. Electrochem. Soc.*, 2017, **164**, F418.
52 N. Kumano, K. Kudo, Y. Akimoto, M. Ishii and H. Nakamura, *Carbon*, 2020, **169**, 429–439.
53 M. B. Dixit, B. A. Harkey, F. Shen and K. B. Hatzell, *J. Electrochem. Soc.*, 2018, **165**(5), F264.
54 T. Lazaridis, B. M. Stühmeier, H. A. Gasteiger and H. A. El-Sayed, *Nat. Catal.*, 2022, **5**, 363–373.
55 K. Shinozaki, J. W. Zack, R. M. Richards, B. S. Pivovar and S. S. Kocha, *J. Electrochem. Soc.*, 2015, **162**(10), F1144.
56 T. Rundlöf, M. Mathiasson, S. Bekiroglu, B. Hakkarainen, T. Bowden and T. Arvidsson, *J. Pharm. Biomed. Anal.*, 2010, **52**, 645–651.
57 A. Alvarez-Murillo, J. A. Libra and K. S. Ro, *Therm. Sci. Eng. Prog.*, 2022, **30**, 101241.
58 M. Lucian and L. Fiori, *Energies*, 2017, **10**, 211.
59 M. J. Antal Jr., W. S. Mok and G. N. Richards, *Carbohydr. Res.*, 1990, **199**, 91–109.
60 B. Girisuta, L. P. B. M. Janssen and H. J. Heeres, *Chem. Eng. Res. Des.*, 2006, **84**, 339–349.
61 I. van Zandvoort, Y. Wang, C. B. Rasrendra, E. R. van Eck, P. C. Bruijnincx, H. J. Heeres and B. M. Weckhuysen, *ChemSusChem*, 2013, **6**, 1745–1758.
62 S. K. R. Patil and C. R. F. Lund, *Energy Fuels*, 2011, **25**, 4745–4755.
63 M. T. Reza, W. Becker, K. Sachsenheimer and J. Mumme, *Bioresour. Technol.*, 2014, **161**, 91–101.
64 C. Falco, N. Baccile and M.-M. Titirici, *Green Chem.*, 2011, **13**, 3273–3281.
65 C. Brett and K. Waldron, in *Physiology and Biochemistry of Plant Cell Walls*, ed. C. Brett and K. Waldron, Springer Netherlands, Dordrecht, 1990, pp. 4–57.
66 D. W. S. Wong, in *Mechanism and Theory in Food Chemistry*, ed. D. W. S. Wong, Springer International Publishing, Cham, 2nd edn, 2018, pp. 123–168.
67 D. Ren, X. Jiang, N. Zhang, J. Duo, K. Norinaga and Z. Huo, *Biomass Convers. Biorefin.*, 2023, **13**, 8115–8121.
68 T. Shibamoto and R. A. Bernhard, *Agric. Biol. Chem.*, 1977, **41**, 143–153.
69 F. J. Hidalgo, C. M. Lavado-Tena and R. Zamora, *J. Agric. Food Chem.*, 2020, **68**, 5448–5454.
70 H. Tsuchida, M. Kōmoto, H. Kato and M. Fujimaki, *Agric. Biol. Chem.*, 1973, **37**, 403–409.
71 G. Machell and G. N. Richards, *J. Chem. Soc. (Resumed)*, 1960, 1938–1944.
72 R. Zhang, A. Eronen, X. Du, E. Ma, M. Guo, K. Moslova and T. Repo, *Green Chem.*, 2021, **23**, 5481–5486.
73 A. B. Bjerre and E. Soerensen, *Ind. Eng. Chem. Res.*, 1992, **31**, 1574–1577.
74 G. Pipitone, G. Zoppi, S. Ansaloni, S. Bocchini, F. A. Deorsola, R. Pirone and S. Bensaid, *Chem. Eng. J.*, 2019, **377**, 120677.
75 F. Yue, J. Zhang, C. M. Pedersen, Y. Wang, T. Zhao, P. Wang, Y. Liu, G. Qian and Y. Qiao, *ChemistrySelect*, 2017, **2**, 583–590.
76 N. Paksung, J. Pfersich, P. J. Arauzo, D. Jung and A. Kruse, *ACS Omega*, 2020, **5**, 12210–12223.
77 D. Knežević, W. van Swaaij and S. Kersten, *Ind. Eng. Chem. Res.*, 2010, **49**, 104–112.
78 X. Cao, L. Zhong, X. Peng, S. Sun, S. Li, S. Liu and R. Sun, *Bioresour. Technol.*, 2014, **155**, 21–27.
79 E. Yaman and N. Özbay, *J. Energy Inst.*, 2023, **111**, 101419.
80 J. Zhao, W. Xiuwen, J. Hu, Q. Liu, D. Shen and R. Xiao, *Polym. Degrad. Stab.*, 2014, **108**, 133–138.
81 W.-H. Chen, Y.-S. Chu, J.-L. Liu and J.-S. Chang, *Energy Convers. Manage.*, 2018, **160**, 209–219.
82 A. K. Vasiliou, J. H. Kim, T. K. Ormond, K. M. Piech, K. N. Urness, A. M. Scheer, D. J. Robichaud, C. Mukarakate, M. R. Nimlos, J. W. Daily, Q. Guan, H.-H. Carstensen and G. B. Ellison, *J. Chem. Phys.*, 2013, **139**, 104310.
83 F. A. Stevie and C. L. Donley, *J. Vac. Sci. Technol., A*, 2020, **38**(6), 063204.
84 A. J. Barlow, S. Popescu, K. Artyushkova, O. Scott, N. Sano, J. Hedley and P. J. Cumpson, *Carbon*, 2016, **107**, 190–197.
85 P. Klar, E. Lidorikis, A. Eckmann, I. A. Verzhbitskiy, A. C. Ferrari and C. Casiraghi, *Phys. Rev. B: Condens. Matter Mater. Phys.*, 2013, **87**, 205435.
86 D. Pantea, H. Darmstadt, S. Kaliaguine and C. Roy, *Appl. Surf. Sci.*, 2003, **217**, 181–193.
87 S. Reiche, N. Kowalew and R. Schlögl, *ChemPhysChem*, 2015, **16**, 579–587.
88 K. Kaur and U. G. Phutela, *Paddy Water Environ.*, 2016, **14**, 113–121.
89 D. M. Le, H. R. Sørensen and A. S. Meyer, *Process Biochem.*, 2017, **55**, 126–132.
90 H. N. Tran, C. K. Lee, T. V. Nguyen and H. P. Chao, *Environ. Technol.*, 2018, **39**, 2747–2760.
91 J. W. Straten, P. Schleker, M. Krasowska, E. Veroutis, J. Granwehr, A. A. Auer, W. Hetaba, S. Becker, R. Schlögl and S. Heumann, *Chem. – Eur. J.*, 2018, **24**, 12298–12317.
92 G. H. Major, N. Fairley, P. M. A. Sherwood, M. R. Linford, J. Terry, V. Fernandez and K. Artyushkova, *J. Vac. Sci. Technol., A*, 2020, **38**, 061203.
93 R. Blume, D. Rosenthal, J.-P. Tessonnier, H. Li, A. Knop-Gericke and R. Schlögl, *ChemCatChem*, 2015, **7**, 2871–2881.
94 H. Schmiers, J. Friebel, P. Streubel, R. Hesse and R. Köpsel, *Carbon*, 1999, **37**, 1965–1978.
95 N. Li, H. Li and H. Huang, *Materials*, 2025, **18**, 2397.
96 B. Fang, N. K. Chaudhari, M.-S. Kim, J. H. Kim and J.-S. Yu, *J. Am. Chem. Soc.*, 2009, **131**, 15330–15338.
97 V. Viswanathan and F. Y.-F. Wang, *Nanoscale*, 2012, **4**, 5110–5117.
98 Y. Garsany, O. A. Baturina, K. E. Swider-Lyons and S. S. Kocha, *Anal. Chem.*, 2010, **82**, 6321–6328.
99 A. Caidi, T. Lange, I. Radev, V. Peinecke, F. Özcan and D. Segets, *Part. Part. Syst. Charact.*, 2025, **42**, e00057.
100 K. Shinozaki, J. W. Zack, S. Pylypenko, B. S. Pivovar and S. S. Kocha, *J. Electrochem. Soc.*, 2015, **162**, F1384.

101 Y. Garsany, J. Ge, J. St-Pierre, R. Rocheleau and K. E. Swider-Lyons, *J. Electrochem. Soc.*, 2014, **161**, F628.
102 T. R. Ralph, G. A. Hards, J. E. Keating, S. A. Campbell, D. P. Wilkinson, M. Davis, J. St-Pierre and M. C. Johnson, *J. Electrochem. Soc.*, 1997, **144**, 3845.
103 J. C. Meier, C. Galeano, I. Katsounaros, J. Witte, H. J. Bongard, A. A. Topalov, C. Baldizzone, S. Mezzavilla, F. Schüth and K. J. J. Mayrhofer, *Beilstein J. Nanotechnol.*, 2014, **5**, 44–67.
104 T. Shinagawa, A. T. Garcia-Esparza and K. Takanabe, *Sci. Rep.*, 2015, **5**, 13801.
105 A. Holewinski and S. Linic, *J. Electrochem. Soc.*, 2012, **159**, H864.
106 F. Hiege, L. M. Sicking, K. Kanokkanchana, P. Cignoni, V. Dudarev, A. Ludwig and K. Tschulik, *ACS Electrochem.*, 2025, **1**, 2149–2155.
107 G. Li, A. Iakunkov, N. Boulanger, O. A. Lazar, M. Enachescu, A. Grimm and A. V. Talyzin, *RSC Adv.*, 2023, **13**, 14543–14553.
108 P. Lawtae and C. Tangsathitkulchai, *Molecules*, 2021, **26**, 6521.